Monthly Notices of the ROYAL ASTRONOMICAL SOCIETY

MNRAS **543,** 4235–4253 (2025) https://doi.org/10.1093/mnras/staf1701
Advance Access publication 2025 October 6

Photometric characterization of near-Earth objects from OASI and CASLEO observations

W. Pereira ,[1]★ P. Arcoverde ,[1] M. Melita,[2,3,4] L. Mammana,[2,5] E. Rondón ,[1] J. Michimani ,[1] E. Tello-Huanca,[2,5] F. Monteiro ,[1,6] T. Corrêa,[1] R. Degen,[1] T. Rodrigues[1] and D. Lazzaro [1]

[1]*Observatório Nacional, Rua Gal. José Cristino 77, 20921-400 Rio de Janeiro - RJ, Brazil*
[2]*Instituto de Ingeniería y Tecnología, Universidad Nacional de Hurlingham, Av. Gdor. Vergara 2222, B1688 Villa Tesei, Provincia de Buenos Aires, Argentina*
[3]*Complejo Astronómico El Leoncito (CASLEO, CONICET-UNSJ-UNLP-UNC), Av. Argentina 147, San Juan,* ***J5400FJB****, Argentina*
[4]*Facultad de Ciencias Astronómicas y Geofísicas (UNLP), Paseo del Bosque S/N, FWA, B1900 La Plata, Provincia de Buenos Aires, Argentina*
[5]*Instituto de Astronomía y Física del Espacio (CONICET-UBA), CABA, 1428 Buenos Aires, Argentina*
[6]*UNESP – São Paulo State University, CEP 12516-410, Guaratinguetá - SP, Brazil*

Accepted 2025 October 3. Received 2025 October 2; in original form 2025 July 30

ABSTRACT

We present the photometric characterization of 39 NEOs observed between 2021 and 2024 using telescopes at the *Observatório Astronômico do Sertão de Itaparica* (OASI, Brazil) and the *Complejo Astronómico El Leoncito* (CASLEO, Argentina), as part of the IMPACTON project. This study combines rotational light curve, solar phase curve, and multiband photometry to determine key physical parameters, including rotation period, colour indices, taxonomic classification, absolute magnitude, and phase-function parameters. Rotation periods were determined for 26 NEOs, ranging from 2.33 to 19.81 h, with a mean value of 5.13 ± 3.63 h. Some objects exhibit rotation near the spin barrier, suggesting possible cohesion or binarity. Taxonomic classification was performed for 34 NEOs, showing a predominance of the S/Q-complex (50 per cent), followed by the C-complex (23.5 per cent). A catalogue of 2459 NEOs with published taxonomic data was compiled to analyse compositional trends with diameter. The S/Q-complex remains dominant across all size ranges, while the relative abundance of C-complex asteroids increases with size. For 13 targets, phase-function parameters were robustly estimated, corrected for rotational effects. In the G_1–G_2 space, only six objects follow the expected taxonomic trends, while most deviate, indicating possibly distinct surface properties from larger main-belt asteroids. Complete photometric characterization was achieved for 11 NEOs. These findings highlight the importance of systematic photometric surveys of small NEOs, not only for expanding the catalogue of characterized objects and to uncover trends that might inform on the origin and evolution of the smallest members among the Solar system's small bodies.

Key words: methods: data analysis – techniques: photometric – minor planets, asteroids: general.

1 INTRODUCTION

Near-Earth objects (NEOs) are an important population of Solar system bodies in orbits close to Earth, commonly categorized into four distinct groups based on their orbital parameters: Atiras, Amors, Apollos, and Atens, as described by A. Morbidelli et al. (2002). Particular attention has been given to this population, as NEOs are believed to be parent bodies of material that impacts the planets today and may have played a critical role in the delivery of water and organic molecules to the early Earth and other terrestrial planets, a process potentially essential for the emergence of life (D. P. Glavin et al. 2018, L. Piani et al. 2020, T. Nakamura et al. 2023, D. P. Glavin et al. 2025, T. McCoy et al. 2025).

Reliable physical characterization of NEOs is therefore a fundamental goal of planetary science. Understanding their properties is essential for accurately modelling their orbits, including subtle non-gravitational forces such as the Yarkovsky and the YORP effect, and for understanding surface changes caused by space weathering (R. P. Binzel, V. Reddy & T. L. Dunn 2015; T. Hiroi et al. 2023; T. Noguchi 2023). This characterization also supports efforts to dynamically link NEOs to their specific sources in the asteroid belt (W. F. Bottke et al. 2002; S. Greenstreet, H. Ngo & B. Gladman 2012; R. A. Mohamed & A. S. Alhasi 2022; W.-H. Zhou 2024).

In addition to their scientific value in studying the history of the Solar system, NEOs are of great interest for their potential impacts on Earth. Geological evidence from impact craters and recent events such as Tunguska and Chelyabinsk are clear reminders of this ongoing risk (I. Nemchinov, V. Shuvalov & V. Svetsov 2008; V. V. Emel'yanenko & B. M. Shustov 2013). Therefore, studying the physical properties of NEOs is essential for developing effective mitigation methods, such as fragmentation or deflection, of objects that could threaten the biosphere of Earth (D. Perna et al. 2016; Q. Cheng & W. Zhang 2024). Conversely, their orbital closeness makes

★ E-mail: josesilva@on.br

NEOs relatively accessible targets for space missions and sample-return efforts due to the low deltav required to intercept them (S. Ieva et al. 2014). In addition, due to their proximity to Earth's orbit, studying this population becomes particularly interesting for ground-based observations, as it allows for the analysis of smaller Solar system bodies without the need for large telescopes (D. F. Lupishko & M. Di Martino 1998, R. P. Binzel et al. 2002, M. Granvik et al. 2018).

Photometric observations are essential for the characterization of NEOs, enabling the acquisition of light curves, phase curves, and photometric spectra. These data allow for the determination of several physical properties, including rotation period, axis orientation, shape, internal structure, size, albedo indication, colours, and taxonomic type. Several studies have been dedicated to determining these physical properties for objects in the NEOs population, but it has not been possible to determine such properties for most of them.

In recent decades, extensive efforts have been made to discover and characterize NEOs. Discovery programs have greatly increased the known population, although detection efficiency drops off dramatically at smaller scales; while nearly all kilometre-sized NEOs are known, metre-sized objects may number in the millions (P. Tricarico 2017; R. R. Landis, L. Johnson & K. E. Fast 2023; I. Chow & P. G. Brown 2025). According to the JPL Horizons: Small-Body Data base Query[1], the number of known NEOs across all groups as of June 2025 is approximately 38 800. Apollos and Amors constitute the vast majority of this population, while only a few dozen Atiras have been discovered. However, physical characterization lags far behind discovery. It is estimated that less than 10 per cent of known NEOs currently have defined physical properties, a proportion that is rapidly declining as ongoing surveys increasingly discover fainter and smaller objects (J. Deshapriya et al. 2023). The increasing rate of discovery of new NEOs only widens this gap. Therefore, there is an urgent need for dedicated research focused on investigating the physical properties of NEOs, particularly the smaller members of this population.

Contributing to the broader effort to enhance our understanding of the NEOs population, the IMPACTON project has played a key role in determining the physical properties of small Solar system bodies. The main scientific goal of the observatory so far has been the determination of rotation periods, spin axis orientations, shapes, effective diameters, and taxonomic classifications, using light curves, phase curves, and photometric spectra (J. S. Silva & D. Lazzaro 2015; F. Monteiro et al. 2017, 2018a, b, 2020, 2021, 2023; D. Perna et al. 2017; A. Marciniak et al. 2019, 2023; E. Rondón et al. 2019, 2020, 2022; S. Ieva et al. 2022; J. Michimani et al. 2022, 2023a; P. Arcoverde et al. 2023; W. Pereira et al. 2024; P. Arcoverde et al. 2025). However, to a lesser extent, the project has also participated in observations aimed at detecting cometary activity through the analysis of asteroid radial profiles (S. Martino et al. 2019, 2025; M. Evangelista-Santana et al. 2023), in studies of Jupiter Trojans (A. C. Souza-Feliciano et al. 2020), in stellar occultation (E. Rondón-Briceño et al. 2025), and in astrometric observations for the determination and refinement of orbits of specific targets. In this context, our objective is to present the results of new observations conducted at the *Observatorio Astronômico do Sertão de Itaparica* (OASI, Brazil), and at the *Complejo Astronómico El Leoncito* (CASLEO, Argentina) of small NEOs with the aim of determining their rotation period, the absolute magnitude H, $-G_1 - G_2$ parameters of solar phase curve, and their surface colours, which leads to their taxonomic classification.

[1] Available at: https://ssd.jpl.nasa.gov/tools/sbdb_query.html.

This paper is organized as follows. Section 2 details the observations. Section 3 presents data reduction procedures, and the methodology employed to determine physical parameters. Section 4 presents the results and discussion, followed by a summary and some conclusions in Section 5.

2 OBSERVATIONS

The observational data set supporting this study was collected between February 2021 and September 2024, using two facilities: the OASI, as part of the IMPACTON project (D. Lazzaro 2010; E. Rondón et al. 2020), and the Jorge Sahade Telescope (JS, 2.15-m) at the CASLEO, operated under agreement between the *Consejo Nacional de Investigaciones Científicas y Técnicas de la República Argentina* and the National Universities of La Plata, Córdoba, and San Juan.

The OASI employs a 1 m telescope equipped with a 2048 × 2048 pixel and a 1024 × 1024 pixel CCDs (further details can be found in E. Rondón et al. 2020). The JS telescope, in turn, is equipped with a Roper Versarray 2018B CCD with a 2048 × 2048 pixel array, using the focal reducer going a scale of 0.45 arcsec px^{-1}. At OASI, to obtain rotational light curves and phase curves were used R and V filters of the Johnson–Cousins system, while for spectrophotometric measurements the g, r, i, z filters of the Sloan Digital Sky Survey (SDSS) system. All observations conducted at the JS were made exclusively using the Johnson–Cousins BVRI filters. When necessary, the transformation equations provided by K. Jordi, E. K. Grebel & K. Ammon (2006) were applied to convert magnitudes between the Johnson–Cousins and SDSS photometric systems, particularly for the data acquired at JS.

The selected targets are summarized in Table 1, which lists the objects in our sample, including their absolute magnitude H from JPL Horizons and the physical properties found in the literature. Fig. 1 shows the distribution of the sample in the semimajor axis versus eccentricity space. It is important to note that, at the time of observation, the selection criteria prioritized NEOs for which no physical properties had yet been determined. However, subsequent studies have published data on some of these objects.

3 DATA REDUCTION AND ANALYSIS

The raw observational data were processed using standard procedures, including dark-frame subtraction and flat-field correction. Instrumental magnitudes were measured using MPO CANOPUS software developed by Brian Warner (B. Warner 2018). From the instrumental measurements, three types of magnitudes were obtained, each serving distinct scientific purposes: relative magnitudes, for constructing rotational light curve, calibrated (standardized) magnitudes for spectrophotometric analyses, and reduced magnitudes for phase curve and spectrophotometric analyses.

For light curve studies, where the primary goal is to monitor temporal brightness variations due to rotation, relative photometry was used. This technique relies on differential measurements against a selection of stable reference stars (comparison stars) within the same CCD field of view of the target asteroid. Several field stars of brightness similar to the target were typically chosen, and their consistency was cross-checked to ensure that they were not variable. The relative magnitude of the asteroid was then computed as the difference between its instrumental magnitude and the ensemble mean instrumental magnitude of these selected comparison stars. This approach effectively minimizes the impact of first-order atmo-

Table 1. Know physical properties of the observed NEOs.

NEO	Group	H	P (h)	ρ_V	Tax
2202 Pele	Amor	17.0	–	–	–
10860 (1995 LE)	Amor	17.0	–	0.044[a]	–
14827 Hypnos	Apollo PHA	18.8	–	0.22[b]	C[c], V[d], S[w]
27031 (1998 RO4)	Amor	17.9	4.05[e]	–	–
36236 (1999 VV)	Apollo	15.95	2.743[x]	–	X[w]
88264 (2001 KN20)	Amor	17.0	4.76[e]	0.166[a]	S[d], Q[w]
141495 (2002 EZ11)	Apollo PHA	18.5	3.327[f]	0.453[a]	–
152787 (1999 TB10)	Amor	18.6	–	–	S[d]
174050 (2002 CC19)	Amor	17.6	–	–	Sr[g]
187026 (2005 EK70)	Aten	17.4	3.464[d, g], 4.9[h]	–	Sq[c]
187040 (2005 JS108)	Apollo PHA	19.2	–	0.097[i], 0.199[j]	C[c]
242450 (2004 QY2)	Apollo PHA	14.6	7.072[k]	0.362[j], 0.27[l]	–
264993 (2003 DX10)	Apollo PHA	20.4	–	0.141[a]	–
285638 (2000 SO10)	Apollo	17.6	–	–	C[d]
326732 Nice	Amor	17.7	3.463[o], 3.856[p]	0.048[m]	X[n], D[c, m]
417264 (2006 AT2)	Amor	17.1	–	0.062[j]	Cg[m]
417581 (2006 VA3)	Apollo	17.4	–	0.145[q]	–
429733 Gilbertbaker	Amor	16.6	2.649[r]	0.225[a]	–
439437 (2013 NK4)	Apollo PHA	18.9	–	–	S[d]
480824 (1999 JO6)	Amor	16.6	–	–	–
481032 (2004 YZ23)	Amor	15.2	–	0.025[q]	C[c]
495858 (2003 MJ4)	Apollo	18.8	–	0.419[q]	Q[c]
620082 (2014 QL433)	Apollo PHA	19.9	–	–	–
620102 (2017 QM18)	Amor	18.6	–	0.09[q], 0.274[a]	–
675797 (2016 AX147)	Amor	17.5	–	–	–
756710 (2020 GN3)	Amor	19.2	–	–	–
2004 UV1	Apollo PHA	17.8	–	–	–
2008 WL60	Amor	17.9	2.608[s]	–	S[d, w]
2011 GA	Apollo PHA	20.7	–	–	–
2011 YQ10	Amor	19.1	4.827[t]	–	–
2012 QG8	Amor	19.1	–	–	–
2013 PV2	Amor	20.1	–	0.335[a]	–
2017 UW42	Amor	17.9	–	–	V[d], C[w]
2019 AV4	Amor	17.8	–	–	–
2019 AZ13	Amor	19.6	–	–	V[d], S[w]
2020 DB5	Amor PHA	19.2	5.24[e], 1.54[h]	–	–
2020 JD	Apollo	19.9	–	–	–
2021 JQ24	Amor	17.8	20.923[u]	–	–
2021 MO1	Amor	18.5	5.70[e]	–	S[v]

[a] J. R. Masiero et al. (2021).
[b] D. E. Trilling et al. (2016).
[c] R. P. Binzel et al. (2019).
[d] A. V. Sergeyev & B. Carry (2021).
[e] W. Pereira et al. (2024).
[f] D. Polishook (2012).
[g] V. Benishek (2024).
[h] L. Franco et al. (2024).
[i] J. R. Masiero et al. (2017).
[j] A. K. Mainzer et al. (2019).
[k] M. A. Miftah et al. (2024).
[l] C. R. Nugent et al. (2015).
[m] N. G. Simion et al. (2021).
[n] C.-H. Lin et al. (2018).
[o] P. Pravec et al. (2021).
[p] B. D. Warner & R. D. Stephens (2022b).
[q] J. R. Masiero et al. (2020).
[r] B. D. Warner & R. D. Stephens (2020a).
[s] B. A. Skiff et al. (2019).
[t] B. D. Warner & R. D. Stephens (2022a).
[u] B. D. Warner & R. D. Stephens (2022c).
[v] J. Michimani et al. (2023b).
[w] A. V. Sergeyev et al. (2023).
[x] B. D. Warner & R. D. Stephens (2020b).

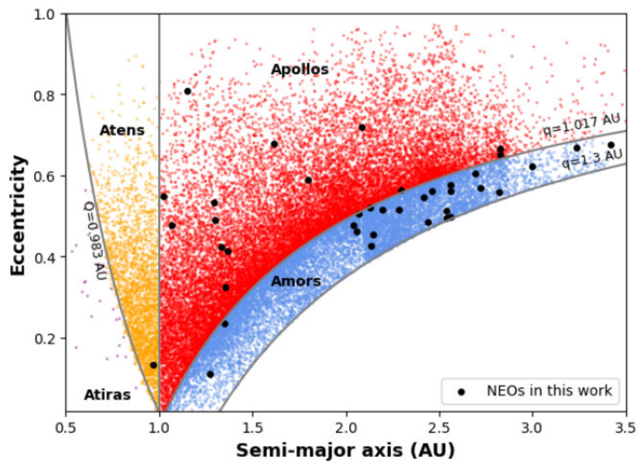

Figure 1. Distribution of the studied NEOs in the semimajor axis versus eccentricity space.

spheric extinction variations and subtle instrumental drifts that are common to both the target and the reference stars.

To determine the reduced magnitude for constructing phase curves and photometric spectra, a standardization procedure was applied. Depending on the scientific objective and the availability of reference stars in the field, we used different photometric catalogues. For the construction of phase curves, the calibrated magnitudes of field stars were obtained from either the *Gaia* DR3 catalogue – transformed into the Johnson–Cousins system using the relations from M. Riello et al. (2021) – or from the Pan-STARRS DR1 catalogue, using the transformations from A. Kostov & T. Bonev (2018) to convert to the same photometric system. For the spectrophotometric analysis, the Pan-STARRS DR1 catalogue was used consistently, with magnitudes converted into the SDSS system following the equations given by J. L. Tonry et al. (2012).

Once the magnitudes of the selected field stars are converted to the appropriate standard photometric system ($m_{\rm cat,field}$), a photometric zero-point (ZP) is calculated for each image or set of images. The ZP represents the average difference between the instrumental magnitudes ($m_{\rm inst,field}$) of the reference stars and their respective transformed catalogued magnitudes:

$$\mathrm{ZP} = \langle m_{\rm inst,field} - m_{\rm cat,field} \rangle. \quad (1)$$

The calibrated magnitude of the asteroid ($m_{\rm cal,ast}$) is then obtained by applying this ZP to the asteroid's instrumental magnitude ($m_{\rm inst,ast}$), measured concurrently:

$$m_{\rm cal,ast} = m_{\rm inst,ast} - \mathrm{ZP}. \quad (2)$$

This $m_{\rm cal,ast}$ is the asteroid's apparent magnitude in the standard photometric system at the time of observation. To allow for the comparison of observations obtained at different epochs and observational geometries, the calibrated magnitude is subsequently converted to the reduced magnitude ($m(\alpha)$). This represents the brightness the asteroid would have if it were located at one astronomical unit from both the Earth and the Sun, and observed at solar phase angle at the moment of observation (α). The reduced magnitude is calculated from the calibrated magnitude as follows:

$$m(\alpha) = m_{\rm cal,ast} - 5\log(r\Delta), \quad (3)$$

where r and Δ are, respectively, the heliocentric and geocentric distances of the asteroid in astronomical units at the instant of observation. This reduced magnitude, $m(\alpha)$, from here we will denoted as $H(\alpha)$), is the fundamental quantity used for subsequent physical analyses.

3.1 Obtaining physical properties

The fundamental observable of a celestial object is its brightness, or magnitude, in a specific filter. However, unlike stellar objects, small bodies merely reflect incident sunlight, and their brightness depends on various physical and geometric parameters. These include their heliocentric and geocentric distances, the illuminated fraction of their surface visible from Earth expressed by the solar phase angle, (α), the visible cross-sectional area (dependent on the aspect angle), as well as intrinsic properties such as shape, composition (and/or albedo), and the microphysical structure of their surface regolith. By analysing how the magnitude varies with time, illumination (solar phase angle), and wavelength, we can determine various physical properties of the body.

3.1.1 Rotational light curve

Rotational light curves tracks temporal variations in brightness due to the changing projected cross-section of an irregularly shaped, rotating object. This variation is therefore periodic, and a Fourier series fit can yield the object's rotation period under the assumption that the variations arise solely from its shape, that the body has a constant albedo, and that it rotates around its minimum energy axis. Under these conditions, the rotation period can be determined using the equation described by A. W. Harris et al. (1989):

$$R(\alpha, t) = A_0 + \sum_{l=1}^{n}\left[A_l \sin\frac{2\pi l}{P}(t-t_0) + B_l \cos\frac{2\pi l}{P}(t-t_0)\right], \quad (4)$$

where $R(\alpha, t)$ is the reduced magnitude at phase angle α and time t, A_0 is the reduced magnitude at a phase angle, A_l and B_l are the Fourier coefficients, P is the series period, t_0 is the mid-point of the observation interval, and n is the degree of the series.

3.1.2 Solar phase curve

In addition to rotational variability, the reduced magnitude also varies with solar phase angle, producing what is known as the phase curve. It should be noted that, by definition, the absolute magnitude H of a small body its reduced magnitude at zero phase angle. However, as it is challenging to observe these objects in opposition (i.e. at zero phase angle), the common approach is to extrapolate the reduced magnitude obtained at various phase angles. Although the general trend shows a decrease in magnitude from large to small phase angles, this decline is non-linear, and a sharp increase – termed the opposition effect – occurs near zero phase angle. This effect arises from sunlight scattered on the surface, which depends on factors such as albedo, grain size of the regolith, surface topography, and others. Conversely, understanding how light is reflected and scattered provides insights into the surface composition, since distinct minerals yield phase curves with different slopes and opposition effects (E. Bowell & K. Lumme 1979).

The IAU adopted a new system, called H-G_1-G_2 (K. Muinonen et al. 2010) in 2012 to improve the modelling of phase curves for high- and low-albedo asteroids. The model is expressed by equation (5), fitted to data using linear least squares:

$$H(\alpha) = H_0 - 2.5\log[G_1\phi_1(\alpha) + G_2\phi_2(\alpha) - (1 - G_1 - G_2)\phi_3(\alpha)], \quad (5)$$

where H_0, G_1, and G_2 are model parameters. The functions $\phi_1(\alpha)$ and $\phi_2(\alpha)$ relate to the linear portion of the phase curve, while $\phi_3(\alpha)$ is associated with the opposition effect. This model allows us to determine both the absolute magnitude and slope parameters indicative of albedo and surface composition for large asteroids (V. G. Shevchenko et al. 2016), however when we analyse smaller asteroids we are unable to estimate albedo of a NEO from its phase curve parameters (P. Arcoverde et al. 2023). Another IAU-recommended model is H-G_1-G_2 developed by A. Penttilä et al. (2016), which employs non-linear least squares. The choice of model to adopt depends on the quality of the data, with the non-linear method proving to be particularly effective for modelling phase curve fits with limited data or large phase angles, as is the case for our NEOs that can exceed 80 degrees.

It is worth noting that the shape of an asteroid, especially if significantly elongated, can strongly influence the observed solar phase curve. This is due to rotational modulation, which introduces variability in the measured brightness depending on the object's orientation at the time of observation. To account for this effect, rotational corrections were applied when appropriate, using light curves acquired simultaneously with the phase curve data. Following the approach described in E. Rondón et al. (2019), the rotational phase was used to compute a correction term, $\Delta V(\phi)$, which was subtracted from the reduced magnitude $H(\alpha)$ to obtain the corrected magnitude $H_c(\alpha)$:

$$\Delta V(\phi) = A\, V(\phi + \phi_0), \tag{6}$$

$$H_c(\alpha) = H(\alpha) - \Delta V(\phi), \tag{7}$$

where $V(\phi + \phi_0)$ represents the rotational light curve at phase $\phi + \phi_0$, and A is the amplitude ratio, following the definition by V. Zappala et al. (1990).

Nevertheless, for objects in our sample where simultaneous light curve data were unavailable, a conservative approach was adopted to estimate the uncertainties in the reduced magnitudes. In particular, for the asteroid 2008 WL60, we applied the light curve amplitude provided in the ALCDEF data base,[2] given that it already has a determined rotational period. For 2017 UW42, which lacks any light curve in the literature, we estimated the rotational contribution by adopting the average amplitude from Asteroid Lightcurve Data base (LCDB; B. D. Warner, A. W. Harris & P. Pravec 2021) for objects within the same size range. In such cases, the maximum uncertainty assigned to each photometric point was computed as the quadrature sum of the photometric error and the estimated rotational amplitude. It is important to highlight that this conservative treatment may overestimate the uncertainties, leading to larger error bars in the derived H-G_1-G_2 fits. None the less, this procedure ensures a more robust estimate of the phase parameters when rotational corrections cannot be applied.

3.1.3 Photometric spectrum

Finally, magnitude also varies with wavelength, as light interacts differently with distinct minerals. Multiband photometry allows for the derivation of both colour indices and photometric spectra. Colour indices are obtained from the magnitude difference in two filters, analysed via 'colour–colour' maps. Photometric spectra are then obtained from reflectances in the filters used (e.g. g, r, i, z), normalized to the r filter, with solar colours removed. For this, calibrated magnitudes were obtained using field stars and adopting $m_g^{\odot} = 5.12 \pm 0.02$, $m_r^{\odot} = 4.68 \pm 0.03$, $m_i^{\odot} = 4.57 \pm 0.04$, and $m_z^{\odot} = 4.54 \pm 0.04$ from the SDSS Data Release 4: Transformations between SDSS magnitudes and $UBVR_cI_c$. Using these solar colours, we obtained the reflectances normalized in the r band, and through the Monte Carlo method, we estimated the errors for the fluxes. Equation 8 shows the normalized reflectance in the SDSS r band for each filter X:

$$R_N = 10^{-0.4\left[(m_X - m_r) - (m_X - m_r)_{\odot}\right]}, \tag{8}$$

where $m_X - m_r$ is the asteroid's colour, and $(m_X - m_r)_{\odot}$ is the solar colour.

Significant physical processes can be identified through correlations in colour index distributions, and numerous taxonomies have been developed based on colours (D. J. Tholen 1984, J. M. Carvano et al. 2010). Photometric spectra, in turn, enable taxonomic classification by comparing the shape to spectral templates.

We determined the taxonomic classification of our targets from their $griz$ photometric spectra. Our methodology relies on a dual approach combining graphical and quantitative analyses. The primary framework follows the methodology of F. E. DeMeo & B. Carry (2013), which uses strict limits on the overall spectral slope (gri-slope) and the 1-μm band depth proxy ($i - z$ colour) to classify objects into ten broad complexes: A, B, C, D, K, L, Q, S, V, and X. This graphical classification is complemented by a quantitative analysis where the photometric reflectance spectrum of each object is compared with templates from F. E. DeMeo et al. (2009), which were interpolated to the central wavelengths of the SDSS filters. The definitive classification for each object was established by identifying the taxonomic class that yielded the minimum chi-square (χ^2) value in the template-fitting process. It is important to note that a taxonomic class provides an indication of surface composition based on spectral characteristics and does not necessarily correspond to a specific mineralogy.

4 RESULTS AND DISCUSSION

We analysed a sample of 39 NEOs for which we obtained a set of physical properties based on photometric observations. Our study covers the determination of rotation periods, absolute magnitudes, phase-function parameters, colour indices, and taxonomic classifications aiming to better assess the physical and compositional diversity within the NEO population.

The obtained results are summarized in Table 3, where for each NEO, when determined, the following parameters are provided: the rotation period (P), the light curve amplitude (A), the absolute magnitude in the V filter (H_0) [with the exception of 429 733 Gilbertbaker for which the absolute magnitude is given in the R filter], the phase curve slope parameters (G_1 and G_2), the colours ($g - r, r - i, i - z$), the estimated diameter (D), and the taxonomy type (Tax). For objects in our sample lacking a directly measured geometric albedo and absolute magnitude, diameters were estimated using the absolute magnitude from JPL Horizons and the mean albedo corresponding to their respective taxonomic class, as presented by M. Mahlke, B. Carry & P. A. Mattei (2022). The overall effective diameter distribution of our observed sample of 39 NEOs is illustrated in Fig. 2, which shows a concentration towards objects primarily in the kilometre and sub-kilometre size ranges. Specifically, the sample presents a mean diameter of 1.22 km, a median of 0.76 km. Approximately 68 per cent of the observed objects fall within the diameter range of 0.36–1.94 km.

[2]Avaliable at: https://alcdef.org/.

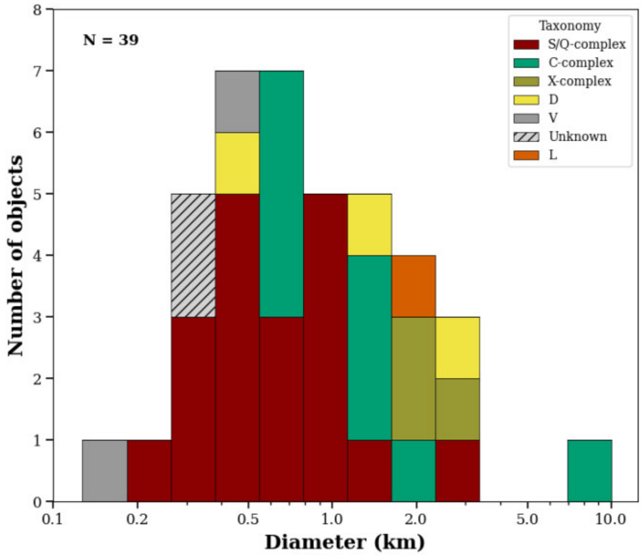

Figure 2. Diameter distribution of the 39 NEOs observed in this work by taxonomic class. The stacked histogram shows the number of objects within logarithmic diameter bins, divided according to the different taxonomic classes as indicated in the legend. Objects with no taxonomic classification are represented by the hatched pattern and an albedo of 0.24 was used to estimate their diameter.

Fig. A1 shows the light curves with the best-fitting Fourier series and the obtained rotation periods. In Fig. A2, we present the photometric reflectance spectra obtained for each asteroid (black line and points). The taxonomic classification models from F. E. DeMeo et al. (2009), adapted to SDSS filters and with the lowest chi-square value, are represented by the red dashed line with the envelope of their respective standard deviations. Finally, Fig. A3 shows the phase curve plots and their best fits.

4.1 Rotational properties and internal structure

We determined the rotation period for a sample of 26 NEOs, spanning values from 2.33 to 19.81 h, and a mean period of approximately 5.13 ± 3.63 h. The distribution of these periods is presented in Fig. 3. Notably, the majority of objects (16 out of 26) exhibit periods shorter than 5 h, indicating a significant fraction of relatively rapidly rotating bodies within our sample. Light curve amplitudes range from 0.07 to 1.40 mag, with a mean amplitude of 0.27 mag, suggesting a variety of shapes from nearly spheroidal to significantly elongated bodies, assuming principal-axis rotation and minimal surface albedo heterogeneity.

Fig. 4 shows our obtained rotation periods (red triangles) plotted against estimated diameters, alongside the broader population of small bodies given in the LCDB. The spin barrier at approximately 2.2 h, indicated by the red dotted line, corresponds to the critical rotation period below which strengthless, rubble-pile asteroids with bulk densities near 2 g/cm^3 would undergo structural failure due to centrifugal forces (P. Pravec & A. W. Harris 2000). Objects larger than roughly 250 m are generally unable to maintain such short periods without disruption, implying that self-gravity dominates their structural cohesion (A. W. Harris 1996). In these cases, rotational disruption or surface mass-loss can occur, potentially leading to the formation of binary systems (K. J. Walsh, D. C. Richardson & P. Michel 2012; J. Wimarsson et al. 2024).

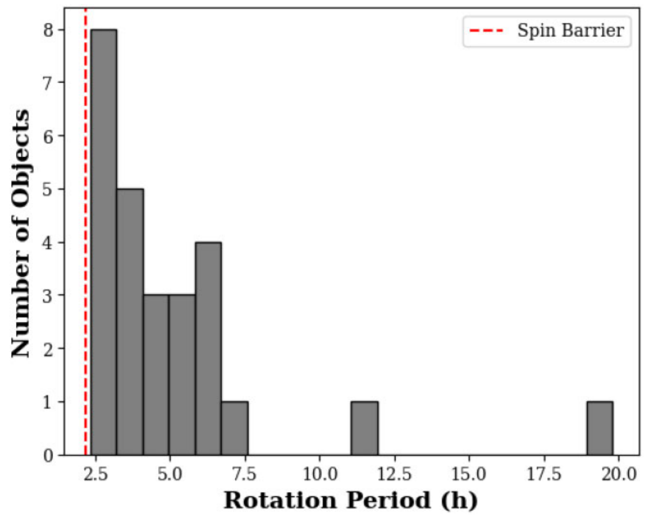

Figure 3. Histogram showing the distribution of rotation periods for the 26 NEOs studied in this work. The dashed line indicates the conventional spin barrier at 2.2 h.

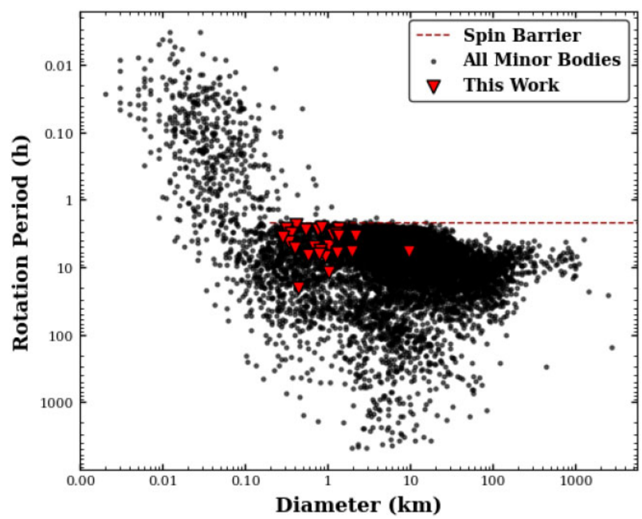

Figure 4. Distribution of NEO Rotation Periods versus Diameter. Point symbols represent asteroids with rotation periods and quality index $U > 2$ from the LCDB. The triangles represent the NEOs presented in this work.

Periods shorter than 5 h, as observed in most of our sample, reflect a population that includes both gravitational aggregates with modest cohesion and coherent monolithic fragments. Smaller asteroids below the 250 m threshold can rotate faster than the spin barrier due to their material strength, while larger bodies near this limit may possess weak cohesion or be close to rotational disruption (P. Pravec & A. W. Harris 2000; K. A. Holsapple 2007). This diversity in rotation rates reflects varied internal structures and evolutionary histories, including collisional fragmentation and YORP-driven spin evolution (P. Pravec, A. W. Harris & T. Michalowski 2002).

Some asteroids in our data set – namely 14 827 Hypnos, 141 495 (2002 EZ11), 174 050 (2001 CC19), 326 732 Nice, 429 733 Gilbert-baker, 480 824 (1999 JO6), 495 858 (2003 MJ4), 675 797 (2016 AX147), 2004 UV1, 2011 YQ10, 2012 QG8, 2019 AV4, and 2020 JD – lie close to the spin barrier. While their proximity to this limit makes them strong binary candidates, it is important to note that this alone does not confirm their binary nature. Rotational fission near

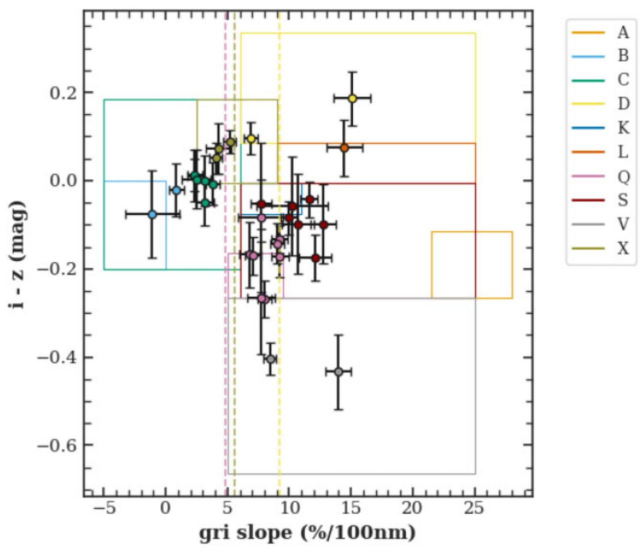

Figure 5. Colours $i - z$ versus *gri-slope* for asteroids with taxonomic data from this work. The boxes represent taxonomic class boundaries from F. E. DeMeo & B. Carry (2013).

the spin barrier is a well-established mechanism for binary formation (K. J. Walsh, D. C. Richardson & P. Michel 2008), and the confirmed binary status of 326 732 Nice (B. D. Warner & R. D. Stephens 2022b) supports this interpretation. Alternatively, these objects could possess sufficient internal cohesion or be near rotational disruption, leading to similar rotational characteristics.

NEOs in the 0.3–2 km diameter range occupy an intermediate regime and remains underrepresented in detailed rotational studies, limiting constraints on spin evolution models (P. Pravec et al. 2012; D. Polishook et al. 2016; J. Ďurech & J. Hanuš 2018; F. Monteiro et al. 2020). Our sample, which predominantly covers this size range, provides new data to help fill this gap. This size domain bridges small monolithic bodies, whose structural integrity is dominated by material strength, and larger rubble-pile asteroids held together primarily by self-gravity. However, recent findings show that this dichotomy is an oversimplification; weak but significant cohesive forces (∼10–100 Pa) likely play a crucial role in maintaining the structural integrity of rapidly rotating spoil piles that would otherwise be beyond the rotational failure limit (B. Rozitis, E. Maclennan & J. P. Emery 2014; P. Sánchez & D. J. Scheeres 2014; F. Monteiro et al. 2023; B. Cheng & H. Baoyin 2024). Understanding rotational properties in this regime is fundamental to model asteroid disruption, binary formation via YORP-induced rotational fission, and surface regolith dynamics, as directly observed on asteroids such as Bennu and Ryugu (D. J. Scheeres 2015; O. S. Barnouin et al. 2019; E. R. Jawin et al. 2020; J. Brisset et al. 2022).

4.2 Photometric spectrum and taxonomic distribution of NEOs

The taxonomic classification was determined for 34 NEOs based on their photometric spectra, following the methodology outlined above. In Fig. 5, is given the distribution of our targets in the gri-slope versus $i - z$ colour space according to F. E. DeMeo & B. Carry (2013). It is noteworthy a general agreement, with objects populating the domains corresponding to their final classification. Individual reflectance spectra and their best-fitting templates are given in Fig. A2.

The observed sample includes diverse taxonomic types, with a clear predominance of asteroids exhibiting silicate-rich spectral characteristics. The most common classes being the Q-type, with nine objects, the S-type with six, and the Sq- and Sr-types with only one object each. Quite a significant portion of the sample presents flatter and more neutral spectra, representative of the C-complex, which includes B-, C-, and Cg-types, and accounting for a total of eight objects, plus other three objects of the X-complex. We also found three D-type asteroids, two V-type, and one L-type.

To evaluate the reliability of our photometric classifications, we conducted two validation tests. First, we compared our results with published classifications for objects that are common to our sample (see Table 1). The comparison shows a high degree of consistency in most cases. For instance, our classification of 88 264 (2001 KN20) as an Sq-type is in excellent agreement with its literature assignment within the S/Q-complex. Likewise, our classification of 174 050 (2002 CC19) and 2021 MO1 as S-type asteroids aligns well with their published Sr-type and S-type classifications, respectively.

Special cases with ambiguous literature data were analysed with particular attention. For 14 827 Hypnos, which has conflicting C, V, and S classifications in the literature, our analysis favours a Q-type classification. This result is supported by its moderate albedo of $\rho_V = 0.22$, which tend to confirm its nature as a silicate-rich body. Such consistencies increase our confidence on the classifications determined for those with no taxonomic classification published. We do note some differences, such as for object 36 236 (1999 VV), classified as L-type, whereas in the literature (A. V. Sergeyev et al. 2023) is a X-type. This disagreement may indicate differences in the data, in the analysis methodologies or in the geometric configuration of an inhomogeneous body.

For the second validation test, we used the albedo as an independent constraint to our classification. For instance, 88 264 (2001 KN20), classified as Sq-type, has a known albedo of $\rho_V = 0.166$, consistent with a silicate-rich S-complex composition. Similarly, the very low albedo for 481 032 (2004 YZ23) ($\rho_V = 0.025$) reinforces its classification as a primitive C-type object.

This diagnostic proves to be particularly effective for resolving ambiguities within the X-complex. Although spectrally similar, this group includes classes corresponding to different compositions and albedo: the low-albedo Xc-type, the moderate-albedo Xk-type, and the high-albedo Xe-type according to F. E. DeMeo et al. (2009). The objects 10 860 (1995 LE), 326 732 Nice, and 417 264 (2006 AT2), classified in the X-complex, exhibit low albedo ($\rho_V < 0.07$), suggesting a composition consistent with primitive Xc-type. The use of albedo as a complementary tool significantly enhances the confidence in our final compositional analysis.

For the purpose of statistical analysis we then grouped related classes into broader taxonomic complexes: the S, Sq, Sr, and Q types were merged into the S/Q-complex, while the B, C, and Cg types were grouped into the C-complex. The resulting taxonomic distribution of our sample is illustrated in Fig. 6. The population is clearly dominated by silicate-rich asteroids, with the S/Q-complex representing 50 per cent of the classified objects. The second most abundant group is the C-complex, accounting for 23.5 per cent of the sample. The remaining fractions include X-complex (8.8 per cent), D-type (8.8 per cent), V-type (5.9 per cent), and L-type (2.9 per cent) asteroids.

A comparison of our results with recent taxonomic studies of NEOs reveals both consistencies and interesting differences. The high representation of the S/Q-complex in our sample (50 per cent) is in excellent agreement with the findings by D. Perna et al. (2018) (57 per cent), J. Michimani et al. (2023b) (51.1 per cent), M. Birlan et al. (2024) (45 per cent), and M. A. Barucci et al. (2023) (>40 per cent), reinforcing the consensus that these silicate-rich objects

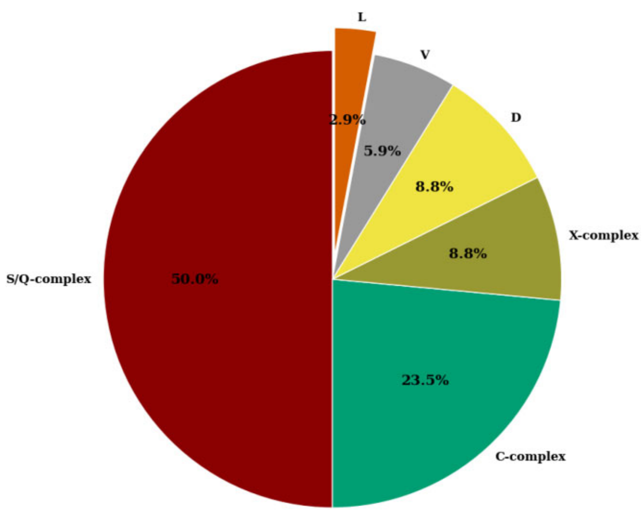

Figure 6. Taxonomic distribution of the 34 NEOs analysed in this work.

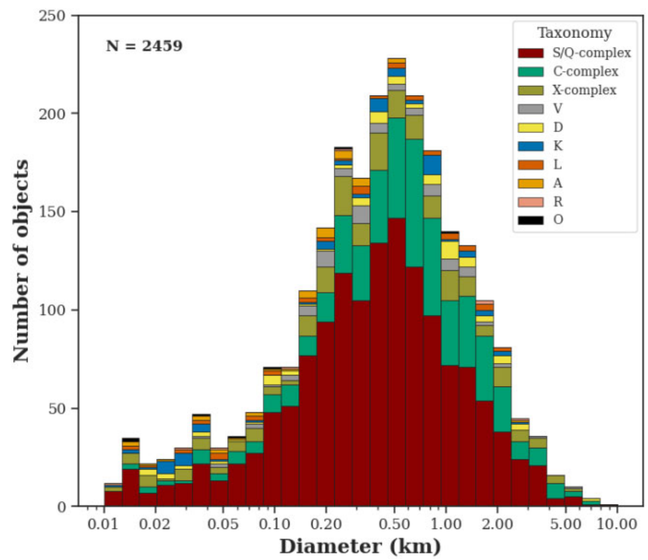

Figure 7. Taxonomic distribution of NEOs from our sample combined with literature data. Stacked histogram showing the number of objects per taxonomic class as a function of the diameter.

are predominant in the NEO population. On the other hand, the proportion of C-complex asteroids in our sample (23.5 per cent) is notably higher than that reported by most of these studies, which found fractions between 9–16 per cent. Our result is, however, comparable to the range of 10–20 per cent reported by M. A. Barucci et al. (2023). Furthermore, we identify abundance in D-type, similar to found by M. A. Barucci et al. (2018), D. Perna et al. (2018), M. Marsset et al. (2022) and J. Michimani et al. (2023b). On the other hand, we did not identify any A-type asteroid, a class found in other samples, which reached a remarkable abundance for small NEOs population (D. Perna et al. 2018; M. Popescu et al. 2018; S. Ieva et al. 2020; J. Michimani et al. 2023b). These differences can likely be attributed to a combination of factors, including small sample statistics, different observational methodologies, and inherent selection biases for each survey.

To mitigate these small-sample effects and analyse population-wide trends, we compiled an extensive data set combining our new classifications with published taxonomies. This comprehensive catalogue includes data from major spectroscopic surveys such as MITHNEOS (R. P. Binzel et al. 2019; M. Marsset et al. 2022) and MANOS (M. Devogèle et al. 2019), as well as from large-scale multiband photometric surveys like SDSS and SkyMapper (A. V. Sergeyev et al. 2023). The compilation is further enriched by data from several other key works in the field (S. Ieva et al. 2018, 2020; D. Perna et al. 2018; M. Popescu et al. 2019; T. Hromakina et al. 2021, 2023; M. Mahlke et al. 2022; J. Michimani et al. 2023b; M. Birlan et al. 2024).

Our final data set comprises 2459 NEOs, with a taxonomic distribution dominated by the S/Q-complex (1444 objects, or 58.7 per cent), followed by the C-complex (498, or 20.3 per cent) and the X-complex (216, or 8.8 per cent). Among the less populous but significant classes, V-type and D-type asteroids are found in nearly equal proportions (72 objects each, or 2.9 per cent), along with a notable population of K-types (65 objects, or 2.6 per cent). The sample is completed by L-type (43, or 1.8 per cent) and A-type (34, or 1.4 per cent) asteroids. For objects in this compiled catalogue lacking a measured geometric albedo, diameters were estimated using the mean albedo for their respective taxonomic class, as provided by M. Mahlke et al. (2022). The resulting taxonomic distribution as a function of diameter for this comprehensive sample is presented in Fig. 7.The distribution reveals several key population-level trends. The S/Q-complex asteroids are the dominant group at all diameters, particularly below 2 km, where their predominance is most pronounced. The C-complex is the second most abundant group overall, and its relative contribution increases progressively with diameter, becoming more comparable to that of S/Q-types above 2 km.

To quantitatively assess the observed trend of increasing C-complex asteroid contribution with size, we calculated the ratio of C-complex to S/Q-complex objects (N_C/N_S) within logarithmic diameter bins from our combined data set. As illustrated in Fig. 8, a strong positive correlation is evident between the C/S ratio and diameter, quantified by a Pearson correlation coefficient of $\rho_{\rm Pearson} = 0.81$. This increasing trend corroborates the hypothesis that the observational underrepresentation of smaller carbonaceous objects, primarily due to their lower albedo, is more pronounced at smaller diameters. This suggests that their intrinsic abundance is likely higher than raw observational counts indicate, especially for larger bodies.

This size-dependent taxonomic distribution reflects well-known observational biases: magnitude-limited surveys are more likely to detect high-albedo S/Q-complex objects than the darker C-complex ones, especially at small sizes. As a result, the observed overrepresentation of silicate-rich bodies likely does not reflect the intrinsic NEO population.

The convergence toward parity at $D \sim 5$ km suggests a more balanced intrinsic ratio, though collisional grinding may deplete carbonaceous fragments below 1 km (F. E. DeMeo & B. Carry 2014; M. Jutzi 2019). The increasing fraction of C-complex asteroids with diameter supports the idea that carbonaceous bodies are more abundant than the observations suggest, as indicated by dynamical models and debiased NEO population estimates (M. Granvik et al. 2018; M. Marsset et al. 2022).

4.3 Phase curves and surface properties

We obtained phase curves for 13 NEOs using the three-parameter H–G_1–G_2 phase-function system K. Muinonen et al. (2010), specifically, we employed the non-linear model developed by A. Penttilä et al. (2016). The resulting curves are presented in Fig. A3. All phase curves were obtained during the same opposition, with the exception

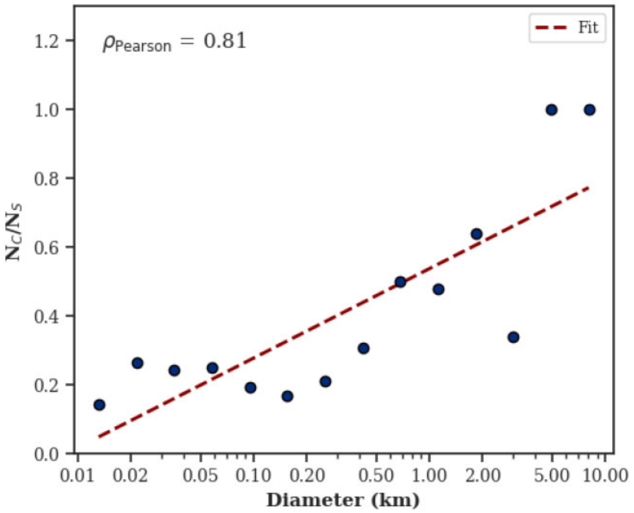

Figure 8. Ratio of C-complex to S/Q-complex asteroids as a function of diameter. The circles represent the $N_\mathrm{C}/N_\mathrm{S}$ ratio (number of C-complex objects divided by the number of S/Q-complex objects) within logarithmic diameter bins, derived from the combined data set of NEOs. The dashed line indicates a linear fit to the data, highlighting the increasing trend of the C/S ratio with diameter.

of object 417581, for which data from different oppositions were utilized. For object 429733, observations were conducted in the *R* band, as *V*-band data covering a sufficient range of phase angles could not be obtained. For three objects: 174050, 417581, and 2011 YQ10, we present new phase curves given in P. Arcoverde et al. (2023) based on multisite observations from both OASI and CASLEO in the *V* band. This data has been corrected for rotational effects.

For the three objects in common with the work of P. Arcoverde et al. (2023) (174050, 417581, and 2011 YQ10), a direct comparison of the G_1 and G_2 parameters reveals some notable differences. The values obtained in both studies, along with their absolute differences ($|\Delta G = G_{\mathrm{This\ work}} - G_{\mathrm{Arcoverde}}|$), are summarized in Table 2. For 174050 (2002 CC19), the parameters are consistent within the uncertainties, whereas for the other two objects, the discrepancies are more significant.

These discrepancies can be attributed to some factors. Firstly, P. Arcoverde et al. (2023) obtained their phase parameters from observations in the Johnson–Cousins *R* filter, whereas our phase curves for these objects were obtained from *V*-band observations. Studies have shown that phase curve slope parameters can be wavelength-dependent; for instance, V. G. Shevchenko et al. (2016) found indications of such variations, and subsequent work has confirmed that the G_1 and G_2 parameters can indeed differ between filters (M. Mahlke, B. Carry & L. Denneau 2021). Secondly, the application of different rotational corrections introduces another source of systematic difference. As shown in equation (6), the correction term, $\Delta V(\phi)$, is directly dependent on the adopted light curve solution, including its period, phasing, and amplitude (A). Our work obtained different rotational period solutions for these objects compared to those used by P. Arcoverde et al. (2023). A change in the derived rotation period directly alters the light curve solution, which in turn impacts the rotational correction applied to the phase curve data and, consequently, the derived phase parameters. The variations in the filters used for the observations, as well as the different period solutions applied for correction, are the main reasons for the discrepancies observed in the obtained phase parameters.

To investigate potential correlations between surface properties and composition, we analysed the distribution of our sample in the G_1–G_2 parameter space (Fig. 9), in comparison with the main-belt asteroids (MBAs) sample from V. G. Shevchenko et al. (2022). Although V. G. Shevchenko et al. (2016) showed that MBAs generally follow a linear trend and occupy preferential regions according to their taxonomy in this space, our NEO data exhibit a broader dispersion. Notably, only five objects in our sample (27031, 326732, 417581, 429733, and 2019 AV4) fall within the expected regions for their corresponding taxonomic types. The remaining objects deviate from these preferred domains, with several clearly positioned outside the established trend.

This discrepancy is consistent with the findings of E. Rondón et al. (2019) and P. Arcoverde et al. (2023), who observed that asteroids smaller than 10 km often exhibit anomalous behaviour in the G_1–G_2 space. A similar behaviour is also evident in polarimetric phase curves. For example, R. Gil-Hutton, C. López-Sisterna & M. F. Calandra (2017) showed that small (D < 11 km) V-type asteroids display a distinct polarimetric phase curve compared to that of (4) Vesta. A possible explanation is that smaller asteroids, due to their lower surface gravity, possess less developed regoliths (S. D. Price 2004), possibly with a deficiency of fine grains (H.-W. Hsu et al. 2022). Such differences in surface texture could directly influence back-scattering properties and shadow-hiding (Y. G. Shkuratov & P. Helfenstein 2001), which is one of the mechanisms that determine the shape of the phase curve. Additionally, a more pronounced macroscopic roughness on these smaller bodies (D. Banik, K. Gaurav & I. Sharma 2022; C. Herrmann & J.-B. Vincent 2024) might also contribute to the observed scatter in the phase curve parameters, which would not be accounted for by the established trends.

Given that our sample consists predominantly of small bodies (D = 0.18–9.43 km), such deviations likely reflect size-dependent surface properties, that are not captured by statistical trends derived from larger main-belt populations. These results highlight the importance of extending phase-curve studies to small NEOs, which may possess

Table 2. Comparison of phase curve parameters for objects in common with P. Arcoverde et al. (2023).

Object	Parameter	This Work	P. Arcoverde et al. (2023)	$\|\Delta G\|$
174050 (2002 CC19)	G_1	0.054 ± 0.012	$0.000^{+0.073}_{-0.000}$	0.05 ± 0.04
	G_2	0.206 ± 0.010	$0.192^{+0.066}_{-0.048}$	0.01 ± 0.06
417581 (2006 VA3)	G_1	0.707 ± 0.090	$0.769^{+0.230}_{-0.240}$	0.06 ± 0.25
	G_2	0.031 ± 0.031	$0.231^{+0.235}_{-0.027}$	0.20 ± 0.14
2011 YQ10	G_1	0.197 ± 0.057	$0.675^{+0.009}_{-0.215}$	0.48 ± 0.13
	G_2	0.463 ± 0.039	$0.325^{+0.217}_{-0.240}$	0.14 ± 0.23

Note. For the calculation of ΔG and its uncertainty, the asymmetric errors from P. Arcoverde et al. (2023) were symmetrized by averaging the upper and lower bounds. The uncertainty in ΔG was calculated via standard error propagation.

Table 3. Obtained physical properties of the observed NEOs. For each object the following physical parameters are provided: rotation period (P) and its uncertainty, light curve amplitude (A), absolute magnitude in the V filter (H_0) and its uncertainty (except for 429 733 Gilbertbaker, which is given in the R filter), phase function parameters G_1 and G_2 with their respective uncertainties, colour indices ($g-r$, $r-i$, $i-z$), estimated diameter (D), and taxonomic classification (Tax). Diameters for objects lacking a measured geometric albedo were estimated using the absolute magnitude from JPL Horizons and the mean albedo for their respective taxonomic class, as provided by M. Mahlke et al. (2022).

Asteroid	P (h)	A (mag)	H_0 (mag)	$G1$	$G2$	$g-r$	$r-i$	$i-z$	D (km)	Tax
2202 Pele	11.652 ± 0.021	0.42	–	–	–	0.597 ± 0.025	0.166 ± 0.027	−0.168 ± 0.074	1.08 ± 0.15	Q
10860 (1995 LE)	–	–	–	–	–	0.530 ± 0.036	0.165 ± 0.029	0.073 ± 0.058	2.50 ± 1.40	X
14827 Hypnos	2.762 ± 0.006	0.11	–	–	–	0.626 ± 0.019	0.142 ± 0.019	−0.169 ± 0.043	0.49 ± 0.19	Q
27031 (1998 RO4)	4.854 ± 0.002	0.09	18.030 ± 0.015	0.3980 ± 0.040	0.2980 ± 0.045	0.642 ± 0.015	0.151 ± 0.017	−0.269 ± 0.042	0.67 ± 0.09	Q
36236 (1999 VV)	–	–	–	–	–	0.708 ± 0.04	0.237 ± 0.037	0.074 ± 0.025	2.02 ± 0.36	L
88264 (2001 KN20)	4.756 ± 0.007	0.20	17.556 ± 0.022	0.0113 ± 0.021	0.6613 ± 0.062	0.633 ± 0.019	0.190 ± 0.018	−0.133 ± 0.031	1.00 ± 0.49	Sq
141495 (2002 EZ11)	2.330 ± 0.001	0.24	–	–	–	0.616 ± 0.022	0.170 ± 0.026	−0.054 ± 0.056	0.40 ± 0.09	S
152787 (1999 TB10)	–	–	–	–	–	0.731 ± 0.025	0.202 ± 0.028	−0.434 ± 0.084	0.46 ± 0.08	V
174050 (2002 CC19)	3.317 ± 0.020	0.10	16.951 ± 0.010	0.0538 ± 0.012	0.2060 ± 0.010	0.703 ± 0.020	0.177 ± 0.019	−0.044 ± 0.04	1.10 ± 0.21	S
187026 (2005 EK70)	6.980 ± 0.001	0.34	–	–	–	0.667 ± 0.015	0.151 ± 0.016	−0.143 ± 0.046	0.91 ± 0.13	Q
187040 (2005 JS108)	–	–	–	–	–	0.548 ± 0.016	0.134 ± 0.017	−0.006 ± 0.049	0.61 ± 0.53	Cg
242450 (2004 QY2)	–	–	–	–	–	0.679 ± 0.020	0.143 ± 0.020	−0.173 ± 0.047	3.20 ± 0.46	Q
264993 (2003 DX10)	–	–	–	–	–	0.630 ± 0.049	0.155 ± 0.062	−0.084 ± 0.169	0.29 ± 0.12	Q
285638 (2000 SO10)	5.503 ± 0.003	1.03	–	–	–	–	–	–	–	–
326732 Nice	3.462 ± 0.003	0.10	17.456 ± 0.021	0.7597 ± 0.025	0.0015 ± 0.011	0.531 ± 0.015	0.190 ± 0.018	0.089 ± 0.025	1.95 ± 0.63	X
417264 (2006 AT2)	5.9300 ± 0.068	0.37	–	–	–	0.513 ± 0.016	0.178 ± 0.017	0.05 ± 0.035	2.08 ± 0.20	X
417581 (2006 VA3)	6.164 ± 0.021	0.45	17.183 ± 0.064	0.7073 ± 0.090	0.0307 ± 0.031	0.519 ± 0.020	0.121 ± 0.021	0.011 ± 0.058	1.27 ± 0.31	C
429733 Gilbertbaker	2.675 ± 0.158	0.17	16.637 ± 0.064*	0.7069 ± 0.029	0.2931 ± 0.042	0.526 ± 0.026	0.155 ± 0.023	–	1.37 ± 0.85	Q?
439437 (2013 NK4)	19.810 ± 0.030	0.50	–	–	–	–	–	–	–	
480824 (1999 JO6)	3.593 ± 0.015	0.46	–	–	–	0.69 ± 0.04	0.269 ± 0.037	0.186 ± 0.025	2.57 ± 0.56	D
481032 (2004 YZ23)	5.762 ± 0.037	0.44	14.749 ± 0.009	0.4346 ± 0.036	0.0735 ± 0.034	0.495 ± 0.022	0.146 ± 0.021	0.012 ± 0.037	9.43 ± 0.56	C
495858 (2003 MJ4)	2.628 ± 0.015	0.17	–	–	–	–	–	–	–	–
620082 (2014 QL433)	6.651 ± 0.037	0.12	19.879 ± 0.004	0.2010 ± 0.006	0.4210 ± 0.053	0.481 ± 0.020	0.116 ± 0.023	−0.02 ± 0.06	0.57 ± 0.20	B
620102 (2017 QM18)	–	–	–	–	–	0.619 ± 0.025	0.204 ± 0.026	-	0.48 ± 0.17	D?
675797 (2016 AX147)	2.603 ± 0.008	0.12	–	–	–	0.640 ± 0.087	0.208 ± 0.065	−0.057 ± 0.112	0.84 ± 0.16	S
756710 (2020 GN3)	6.253 ± 0.049	0.19	–	–	–	0.430 ± 0.086	0.106 ± 0.062	−0.076 ± 0.099	0.77 ± 0.26	B
2004 UV1	2.731 ± 0.005	0.14	–	–	–	0.650 ± 0.019	0.199 ± 0.019	−0.084 ± 0.038	0.75 ± 0.14	S
2008 WL60	–	–	18.350 ± 0.010	0.0973 ± 0.056	0.6587 ± 0.066	0.684 ± 0.025	0.222 ± 0.031	−0.098 ± 0.090	0.58 ± 0.10	S
2011 GA	–	–	–	–	–	0.648 ± 0.016	0.156 ± 0.014	−0.405 ± 0.036	0.18 ± 0.03	V
2011 YQ10	3.186 ± 0.028	0.08	19.282 ± 0.021	0.1971 ± 0.036	0.4630 ± 0.025	0.633 ± 0.029	0.153 ± 0.037	−0.266 ± 0.127	0.38 ± 0.05	Q
2012 QG8	3.187 ± 0.006	0.07	19.463 ± 0.017	0.7008 ± 0.072	0.2825 ± 0.050	0.547 ± 0.021	0.116 ± 0.024	−0.0 ± 0.056	0.76 ± 0.12	Cg
2013 PV2	–	–	–	–	–	0.566 ± 0.022	0.143 ± 0.026	–	0.22 ± 0.06	Q?
2017 UW42	–	–	18.285 ± 0.030	0.7476 ± 0.176	0.2524 ± 0.101	0.511 ± 0.04	0.133 ± 0.037	0.004 ± 0.025	1.31 ± 0.20	C
2019 AV4	3.416 ± 0.010	0.27	18.034 ± 0.027	0.9762 ± 0.017	0.0238 ± 0.032	0.551 ± 0.017	0.214 ± 0.017	0.0970 ± 0.036	1.34 ± 0.29	D
2019 AZ13	4.220 ± 0.070	0.16	–	–	–	–	–	–	–	–
2020 DB5	5.244 ± 0.016	0.16	–	–	–	0.665 ± 0.018	0.227 ± 0.021	−0.175 ± 0.052	0.39 ± 0.07	Sr
2020 JD	3.581 ± 0.002	0.33	–	–	–	–	–	–	–	-
2021 JQ24	–	–	–	–	–	0.543 ± 0.023	0.120 ± 0.025	−0.051 ± 0.052	1.61 ± 0.27	Cg
2021 MO1	–	–	–	–	–	0.651 ± 0.033	0.208 ± 0.041	−0.097 ± 0.112	0.54 ± 0.10	S

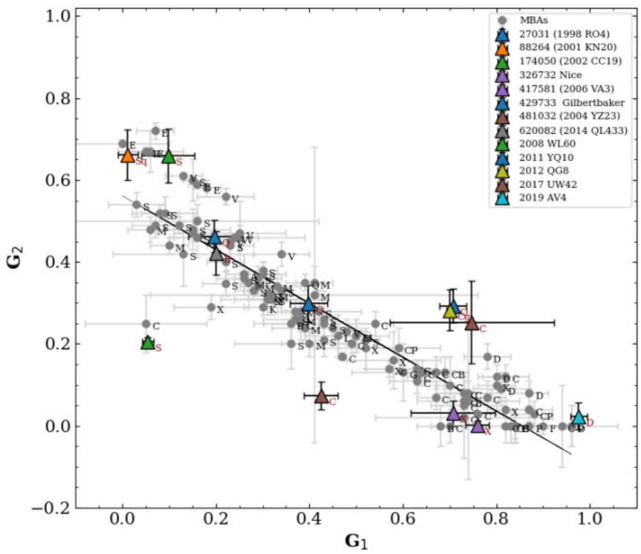

Figure 9. Relationship between the phase-slope parameters G_1 and G_2 for the phase curves. Circles represent the 116 Main Belt Asteroids (MBAs) from V. G. Shevchenko et al. (2022), while geometric symbols correspond to the 13 NEOs analysed in this work. The dashed line indicates the best linear fit to the literature data. Taxonomic types are labelled next to the data points.

fundamentally different photometric and surface characteristics from their main-belt counterparts.

4.4 Complete photometric characterization of NEOs

In this study, we performed a complete photometric characterization for 11 near-Earth asteroids: 27031 (1998 RO4), 88264 (2001 KN20), 174050 (2002 CC19), 326732 Nice, 417581 (2006 VA3), 429733 Gilbertbaker, 481032 (2004 YZ23), 620082 (2014 QL433), 2011 YQ10, 2012 QG8, and 2019 AV4. Our analysis included the determination of rotation periods from light curves, phase curve modelling to determine absolute magnitude and phase parameters (H, G_1, G_2), and extraction of photometric spectra for taxonomic classification.

Phase curves, which are sensitive to asteroid geometry and shape, require rotational corrections based on simultaneously acquired light curves (as per equations 6 and 7) to avoid spurious dispersions, ensuring the precision of H, G_1, G_2 parameters and the correct interpretation of surface properties (E. Rondón et al. 2019). The combination of rotational, phase, and spectral data provides a more robust diagnosis of an object's intrinsic characteristics; for instance, light curve amplitudes, when interpreted in conjunction with taxonomy and phase parameters, can aid in understanding the composition and internal structure. This approach is especially important for smaller NEOs, which are more difficult to detect and for which information is often lacking. Although observationally demanding, complete characterization maximizes the scientific return and helps to clear up ambiguities in the interpretation of physical properties.

5 CONCLUSIONS

We present a detailed photometric characterization of 39 NEOs based on observations conducted at the OASI and CASLEO observatories between 2021 February and 2024 September. Rotation periods were found for 26 objects, with values ranging from 2.33 to 19.81 h (mean 5.13 ± 3.63 h), revealing a relatively large fraction of rapidly rotating bodies. Many small NEOs in the 0.36–1.94 km size range lie near the spin barrier, suggesting cohesive internal structures or potential binary systems. Phase curves were modelled for 13 NEOs, with rotational corrections applied to mitigate shape-related effects and improve the accuracy of H, G_1, and G_2 parameters. Deviations in phase behaviour among smaller objects may reflect size-dependent surface properties.

Photometric spectra enabled taxonomic classification for 34 NEOs, revealing a dominance of the S/Q complex (50 per cent) followed by the C complex (23.5 per cent). These proportions are broadly consistent with the overall NEO population, though our sample exhibits a higher C-complex fraction than some recent studies. Notably, our sample also shows an overabundance of D-type asteroids (8.8 per cent), a finding that is in agreement with recent studies on the taxonomic distribution of NEOs. Conversely, we did not identified any A-type asteroids in our sample, and this absence is likely influenced by the diameter distribution of our objects. This contrasts with previous studies that report a notable abundance of A-type asteroids among the smallest NEOs (diameters ≤ 200 m). It is also important to acknowledge that, despite the new classifications provided, our sample remains relatively small for a robust statistical analysis of taxonomic distributions across the entire NEO population. To mitigate these small-sample effects and analyse population-wide trends, we compiled a catalogue of 2459 NEOs with taxonomic data from the literature, confirming the S/Q dominance across all sizes and a growing C-complex contribution with increasing diameter, highlighting the importance of accounting for observational biases in population analyses.

This work significantly expands the number of NEOs with well-determined physical properties and provides new observational data to improve our understanding of the structural and compositional diversity of these objects. Our integrated approach, combining light curve analysis, phase curve modelling, and photometric spectroscopy, has proven to be effective for a complete physical characterization of NEOs. The obtained results contribute to the broader effort to investigate the nature and evolution of NEOs and offer valuable support for future studies focused in planetary defense.

Building on these results, this study suggests several directions for future observational efforts. To further assess the possible binary nature of objects near the spin barrier, additional photometric monitoring would be valuable, particularly to search for potential mutual events. Where feasible, such data could be complemented by radar observations, which may provide more direct constraints on multiplicity. In addition, visible and near-infrared (VNIR) reflectance spectroscopy is recommended to help clarify uncertain taxonomic classifications and to explore surface mineralogy with greater detail.

ACKNOWLEDGEMENTS

WP, PA, and JM would like to thank the *Coordenação de Aperfeiçoamento de Pessoal de Nível Superior* (CAPES) and the *Conselho Nacional de Desenvolvimento Científico Tecnológico* (CNPq) for their support through various fellowships. ER acknowledge financial support from *Fundação de Amparo à Pesquisa do Estado do Rio de Janeiro* (FAPERJ) (E-26/204.602/2021). DL acknowledges support from CNPq (310964/2020-2) and FAPERJ (E-26/202.001/2021 and E-266/204.276/2024). FM thanks the fellowship granted by *Fundação de Amparo à Pesquisa do Estado de São Paulo* (FAPESP) (2024/16260-6). MM acknowledges funding from *Consejo Nacional de Investigaciones Científicas y Técnicas* (CONICET) PIP 2169/21. The authors are grateful to the IMPACTON team, especially R. Souza, A. Santiago, and A. Henrique, for their technical support. Observations were obtained at the *Observatório do Sertão de Itaparica* (OASI, Itacuruba), operated by the *Observatório Nacional* (ON, Brazil) and at CASLEO, operated under agreement between the *Consejo Nacional de Investigaciones Científicas y Técnicas de la República Argentina* and the National Universities of La Plata, Córdoba and San Juan, proposal code PLP JS-2022B-10. The authors would like to thank the anonymous referee for his comments which significantly improved the paper.

DATA AVAILABILITY

The data underlying this study are available in the article.

REFERENCES

Arcoverde P. et al., 2023, MNRAS, 523, 739
Arcoverde P. et al., 2025, MNRAS, 536, 223
Banik D., Gaurav K., Sharma I., 2022, Proc. R. Soc. A, 478, 20210972
Barnouin O. S. et al., 2019, Nat. Geosci., 12, 247
Barucci M. A. et al., 2018, MNRAS, 476, 4481
Barucci M. A. et al., 2023, Asteroids, Comets, Meteors Conference, LPI Contribution No. 2851, . Lunar and Planetary Institute, Houston, TX, USA, p. 2015
Benishek V., 2024, Minor Planet Bull., 51, 239
Binzel R. P., Lupishko D., di Martino M., Whiteley R. J., Hahn G. J., 2002, Asteroids III. Univ. Arizona Press, Tucson, p. 255
Binzel R. P., Reddy V., Dunn T. L., 2015, Asteroids IV. Univ. Arizona Press, Tucson, p. 243
Binzel R. P. et al., 2019, Icarus, 324, 41
Birlan M. et al., 2024, A&A, 689, A334 https://doi.org/10.1051/0004-6361/202450495
Bottke W. F., Morbidelli A., Jedicke R., Petit J.-M., Levison H. F., Michel P., Metcalfe T. S., 2002, Icarus, 156, 399
Bowell E., Lumme K., 1979, in Gehrels T., Matthews M. S., eds, Asteroids. Univ. Arizona Press, Tucson, p. 132
Brisset J., Sánchez P., Cox C., Corraliza D., Hatchitt J., Madison A., Miletich T., 2022, Planet. Space Sci., 220, 105533
Carvano J. M., Hasselmann P. H., Lazzaro D., Mothé-Diniz T., 2010, A&A, 510, A43
Cheng B., Baoyin H., 2024, MNRAS, 534, 1376
Cheng Q., Zhang W., 2024, Chin. J. Aeronaut., 37, 24
Chow I., Brown P. G., 2025, Icarus, 429, 116444
DeMeo F. E., Carry B., 2013, Icarus, 226, 723
DeMeo F. E., Carry B., 2014, Nature, 505, 629
DeMeo F. E., Binzel R. P., Slivan S. M., Bus S. J., 2009, Icarus, 202, 160
Devogèle M. et al., 2019, AJ, 158, 196
Deshapriya J. et al., 2023, A&A, 674, A50
Ďurech J., Hanuš J., 2018, A&A, 620, A91
Emel'yanenko V. V., Shustov B. M., 2013, Phys.-Usp., 56, 833
Evangelista-Santana M. et al., 2023, MNRAS, 524, 2733
Franco L. et al., 2024, Minor Planet Bull., 51, 289
Gil-Hutton R., López-Sisterna C., Calandra M. F., 2017, A&A, 599, A114
Glavin D. P., Alexander C. M., Aponte J. C., Dworkin J. P., Elsila J. E., Yabuta H., 2018, in Abreu N. , ed., Primitive Meteorites and Asteroids. Elsevier, Amsterdam, the Netherlands, p. 205, https://www.sciencedirect.com/science/article/pii/B9780128133255000033
Glavin D. P. et al., 2025, Nat. Astron., 9, 199
Granvik M. et al., 2018, Icarus, 312, 181
Greenstreet S., Ngo H., Gladman B., 2012, Icarus, 217, 355
Harris A. W., 1996, Lunar Planet. Sci., 27, 493
Harris A. W. et al., 1989, Icarus, 77, 171
Herrmann C., Vincent J.-B., 2024, European Planetary Science Congress. Freie Universität, Berlin, p. EPSC2024–418
Hiroi T. et al., 2023, Icarus, 406, 115755
Holsapple K. A., 2007, Icarus, 187, 500
Hromakina T. et al., 2021, A&A, 656, A89
Hromakina T. et al., 2023, MNRAS, 520, 3143
Hsu H.-W., Wang X., Carroll A., Hood N., Horányi M., 2022, Nat. Astron., 6, 1043
Ieva S. et al., 2014, A&A, 569, A59
Ieva S. et al., 2018, A&A, 615, A127
Ieva S. et al., 2020, A&A, 644, A23
Ieva S. et al., 2022, MNRAS, 513, 3104
Jawin E. R. et al., 2020, J. Geophys. Res. (Planets), 125, e06475
Jordi K., Grebel E. K., Ammon K., 2006, A&A, 460, 339
Jutzi M., 2019, Planet. Space Sci., 177, 104695
Kostov A., Bonev T., 2018, Bulg. Astron. J., 28, 3
Landis R. R., Johnson L., Fast K. E., 2023, 2nd NEO and Debris Detection Conference, . European Space Agency, Darmstadt, Germany, p. 43
Lazzaro D., 2010, Boletin de la Asociacion Argentina de Astronomia La Plata Argentina, 53, 315
Lin C.-H., Ip W.-H., Lin Z.-Y., Cheng Y.-C., Lin H.-W., Chang C.-K., 2018, Planet. Space Sci., 152, 116
Lupishko D. F., Di Martino M., 1998, Planet. Space Sci., 46, 47,55
Mahlke M., Carry B., Denneau L., 2021, Icarus, 354, 114094
Mahlke M., Carry B., Mattei P. A., 2022, A&A, 665, A26
Mainzer A. K., Bauer J. M., Cutri R. M., Grav T., Kramer E. A., Masiero J. R., Sonnett S., Wright E. L., 2019, NEOWISE Diameters and Albedos V2.0. NASA Planetary Data System, urn:nasa:pds:neowise_diameters_albedos::2.0
Marciniak A. et al., 2019, A&A, 625, A139
Marciniak A. et al., 2023, A&A, 679, A60
Marsset M. et al., 2022, AJ, 163, 165
Martino S., Tancredi G., Monteiro F., Lazzaro D., Rodrigues T., 2019, Planet. Space Sci., 166, 135
Martino S. et al., 2025, A&A, 698, A117
Masiero J. R. et al., 2017, AJ, 154, 168
Masiero J. R., Smith P., Teodoro L. D., Mainzer A. K., Cutri R. M., Grav T., Wright E. L., 2020, Planet. Sci. J., 1, 9
Masiero J. R., Mainzer A. K., Bauer J. M., Cutri R. M., Grav T., Kramer E., Pittichová J., Wright E. L., 2021, Planet. Sci. J., 2, 162
McCoy T., Russell S., Zega T., et al., 2025, Nature, 637, 1072
Michimani J. et al., 2022, Minor Planet Bull., 49, 272
Michimani J. et al., 2023a, Minor Planet Bull., 50, 200
Michimani J. et al., 2023b, MNRAS, 526, 2067
Miftah M. A., Ferrais M., Moulane Y., Jehin E., Jabiri A., Benkhaldoun Z., 2024, Minor Planet Bull., 51, 76
Mohamed R. A., Alhasi A. S., 2022, Libyan J. Sci. Technol., 5, 81.
Monteiro F., Silva J. S., Lazzaro D., Arcoverde P., Medeiros H., Souza R., Rodriggues T., 2017, Minor Planet Bull., 44, 20
Monteiro F., Arcoverde P., Medeiros H., Rondon E., Souza R., Rodrigues T., Lazzaro D., 2018a, Minor Planet Bull., 45, 221
Monteiro F., Silva J. S., Lazzaro D., Arcoverde P., Medeiros H., Rodrigues T., Souza R., 2018b, Planet. Space Sci., 164, 54
Monteiro F., Silva J. S., Tamayo F., Rodrigues T., Lazzaro D., 2020, MNRAS, 495, 3990
Monteiro F. et al., 2021, MNRAS, 507, 5403
Monteiro F. et al., 2023, Icarus, 390, 115297
Morbidelli A., Bottke W. F. J., Froeschlé C., Michel P., 2002, Asteroids III. Univ. Arizona Press, Tucson, p. 409
Muinonen K., Belskaya I. N., Cellino A., Delbò M., Levasseur-Regourd A.-C., Penttilä A., Tedesco E. F., 2010, Icarus, 209, 542
Nakamura T. et al., 2023, Science, 379, abn8671
Nemchinov I., Shuvalov V., Svetsov V., 2008, in Adushkin V. V., Nemchinov I. V., eds, Catastrophic Events Caused by Cosmic Objects. Springer, Berlin, p. 1
Noguchi T., 2023, in EGU General Assembly Conference Abstracts, Copernicus Publications, Göttingen, Germany. p. EGU–4647.
Nugent C. R. et al., 2015, ApJ, 814, 117
Penttilä A., Shevchenko V. G., Wilkman O., Muinonen K., 2016, Planet. Space Sci., 123, 117
Pereira W. et al., 2024, Minor Planet Bull., 51, 72
Perna D. et al., 2016, AJ, 151, 14

Perna D., Popescu M., Monteiro F., Lantz C., Lazzaro D., Merlin F., 2017, A&A, 597, A57

Perna D. et al., 2018, Planet. Space Sci., 157, 82

Piani L., Marrocchi Y., Rigaudier T., Vacher L. G., Thomassin D., Marty B., 2020, Science, 369, 1110

Polishook D., 2012, Minor Planet Bull., 39, 187

Polishook D. et al., 2016, Icarus, 267, 243

Popescu M. et al., 2018, MNRAS, 477, 2786

Popescu M. et al., 2019, A&A, 627, A124

Pravec P., Harris A. W., 2000, Icarus, 148, 12

Pravec P., Harris A. W., Michalowski T., 2002, in Bottke W. F., Jr, Cellino A., Paolicchi P., Binzel R. P., eds, Asteroids III. Univ. Arizona Press, Tucson, p. 113

Pravec P. et al., 2012, Icarus, 218, 125

Pravec P. et al., 2021, Cent. Bureau Electron. Telegrams, 5039, 1

Price S. D., 2004, Adv. Space Res., 33, 1548

Riello M. et al., 2021, A&A, 649, A3

Rondón-Briceño E. et al., 2025, Minor Planet Bull., 52, 77

Rondón E., Arcoverde P., Monteiro F., Medeiros H., Navas G., Lazzaro D., Carvano J. M., Rodrigues T., 2019, MNRAS, 484, 2499

Rondón E. et al., 2020, PASP, 132, 065001

Rondón E. et al., 2022, Icarus, 372, 114723

Rozitis B., Maclennan E., Emery J. P., 2014, Nature, 512, 174

Sánchez P., Scheeres D. J., 2014, Meteorit. Planet. Sci., 49, 788

Scheeres D. J., 2015, Icarus, 247, 1

Sergeyev A. V., Carry B., 2021, A&A, 652, A59

Sergeyev A. V. et al., 2023, A&A, 679, A148

Shevchenko V. G. et al., 2016, Planet. Space Sci., 123, 101

Shevchenko V. G. et al., 2022, A&A, 666, A190

Shkuratov Y. G., Helfenstein P., 2001, Icarus, 152, 96

Silva J. S., Lazzaro D., 2015, A&A, 580, A70

Simion N. G., Popescu M., Licandro J., Vaduvescu O., de León J., Gherase R. M., 2021, MNRAS, 508, 1128

Skiff B. A., McLelland K. P., Sanborn J. J., Pravec P., Koehn B. W., 2019, Minor Planet Bull., 46, 458

Souza-Feliciano A. C. et al., 2020, Icarus, 338, 113463

Tholen D. J., 1984, PhD thesis, Univ. Arizona

Tonry J. L. et al., 2012, ApJ, 750, 99

Tricarico P., 2017, Icarus, 284, 416

Trilling D. E. et al., 2016, AJ, 152, 172

Walsh K. J., Richardson D. C., Michel P., 2008, Nature, 454, 188

Walsh K. J., Richardson D. C., Michel P., 2012, Icarus, 220, 514

Warner B., 2018, MPO Software, MPO Canopus v10.7.7.0., Bdw Publ.https://minplanobs.org/BdwPub/php/mpocanopus.php

Warner B. D., Stephens R. D., 2020a, Minor Planet Bull., 47, 23

Warner B. D., Stephens R. D., 2020b, Minor Planet Bull., 47, 105

Warner B. D., Stephens R. D., 2022a, Minor Planet Bull., 49, 16

Warner B. D., Stephens R. D., 2022b, Minor Planet Bull., 49, 22

Warner B. D., Stephens R. D., 2022c, Minor Planet Bull., 49, 83

Warner B. D., Harris A. W., Pravec P., 2021, Asteroid Lightcurve Database (LCDB) Bundle V4.0, (NASA Planetary Data System, urn:nasa:pds:ast-lightcurve-database::4.0

Wimarsson J., Xiang Z., Ferrari F., Jutzi M., Madeira G., Raducan S. D., Sánchez P., 2024, Icarus, 421, 116223

Zappala V., Cellino A., Barucci A. M., Fulchignoni M., Lupishko D. F., 1990, A&A, 231, 548

Zhou W.-H., 2024, Theses, Université Côte d'Azur, https://theses.hal.science/tel-04902667

APPENDIX A: SUPPLEMENTARY MATERIAL AND OBSERVATIONAL DATA

This Appendix provides supplementary material that complements the analysis and results presented in the main body of this paper. For completeness and transparency of our photometric characterization of NEOs, we include a series of figures illustrating the obtained light curves, photometric spectra, and phase curves, along with detailed tables of the observational circumstances and raw measurement data (Tables A1 and A2).

Table A1. Observational circumstances and SDSS-like reduced magnitudes for the observed NEOs. The table lists the observing site, UT date of observation, heliocentric distance (r), geocentric distance (Δ), solar phase angle (α), estimated visual magnitude (MagV), and reduced magnitudes in the SDSS filters (m_g, m_r, m_i, and m_z).

Asteroid	Observatory	Date UT	r (au)	Δ (au)	α (deg)	MagV	m_g	m_r	m_i	m_z
2202 Pele	OASI	2024-07-31T23:03:01	1.502	0.506	12.8	17.1	18.400 ± 0.019	17.803 ± 0.017	17.637 ± 0.021	17.804 ± 0.071
10860 (1995 LE)	OASI	2024-09-05T05:08:54	1.148	0.374	59.2	17.3	19.427 ± 0.031	18.897 ± 0.018	18.732 ± 0.022	18.659 ± 0.053
14827 Hypnos	OASI	2024-05-15T01:42:22	1.178	0.177	17.2	16.3	20.204 ± 0.015	19.578 ± 0.011	19.435 ± 0.015	19.605 ± 0.04
27031 (1998 RO4)	OASI	2023-07-22T03:20:20	1.231	0.255	29.2	16.6	19.687 ± 0.012	19.045 ± 0.009	18.894 ± 0.015	19.162 ± 0.039
33236 (1999 VV)	CASLEO	2022-03-01T12:31:30	1.222	1.086	50.4	18.4	19.623 ± 0.032	18.914 ± 0.024	18.678 ± 0.028	18.603 ± 0.028
88264 (2001 KN20)	OASI	2023-07-14T23:53:49	1.191	0.177	9.4	14.2	18.495 ± 0.015	17.862 ± 0.012	17.672 ± 0.013	17.805 ± 0.028
141495 (2002 EZ11)	OASI	2023-02-16T04:54:59	1.121	0.182	39.7	16.6	20.394 ± 0.018	19.778 ± 0.014	19.608 ± 0.022	19.661 ± 0.051
152787 (1999 TB10)	OASI	2024-03-16T01:22:00	1.076	0.137	50.6	16.3	21.099 ± 0.02	20.367 ± 0.014	20.166 ± 0.024	20.599 ± 0.081
174050 (2002 CC19)	OASI	2021-02-10T01:22:33	1.143	0.182	28.6	15.5	19.363 ± 0.016	18.659 ± 0.011	18.483 ± 0.015	18.526 ± 0.037
187026 (2005 EK70)	OASI	2024-03-08T00:12:23	1.071	0.178	59.5	15.9	20.028 ± 0.013	19.361 ± 0.009	19.21 ± 0.014	19.353 ± 0.043
187040 (2005 JS108)	OASI	2024-07-01T04:18:19	1.098	0.119	45.0	16.5	21.205 ± 0.013	20.657 ± 0.01	20.523 ± 0.015	20.53 ± 0.046
242450 (2004 QY2)	OASI	2024-04-11T21:54:27	1.152	0.918	56.6	16.8	17.054 ± 0.016	16.375 ± 0.012	16.231 ± 0.016	16.404 ± 0.044
264993 (2003 DX10)	OASI	2024-03-16T03:42:59	1.053	0.086	45.8	17.0	22.805 ± 0.036	22.175 ± 0.034	22.02 ± 0.051	22.104 ± 0.161
326732 Nice	OASI	2021-09-01T01:32:55	1.235	0.229	8.7	15.5	18.354 ± 0.012	17.823 ± 0.008	17.634 ± 0.016	17.545 ± 0.02
417264 (2006 AT2)	OASI	2024-01-16T5:37:45	1.313	0.405	30.1	17.0	18.394 ± 0.013	17.882 ± 0.01	17.704 ± 0.014	17.653 ± 0.032
417581 (2006 VA3)	OASI	2021-02-12T23:11:45	1.272	0.339	28.6	16.8	19.038 ± 0.015	18.519 ± 0.012	18.398 ± 0.017	18.387 ± 0.056
429733 Gilbertbaker	OASI	2023-06-14T07:06:37	1.399	0.551	37.1	17.5	18.565 ± 0.021	17.989 ± 0.015	17.834 ± 0.01	–
480824 (1999 JO6)	CASLEO	2024-06-04T08:03:59	1.449	0.558	31.4	17.5	18.419 ± 0.032	17.729 ± 0.023	17.460 ± 0.028	17.274 ± 0.036
481032 (2004 YZ23)	OASI	2024-07-04T02:01:06	1.605	0.792	31.4	17.0	16.896 ± 0.017	16.401 ± 0.013	16.255 ± 0.016	16.243 ± 0.033
620082 (2014 QL433)	OASI	2023-08-13T23:27:42	1.132	0.120	8.1	16.1	20.781 ± 0.016	20.301 ± 0.013	20.185 ± 0.01	20.206 ± 0.057
620102 (2017 QM18)	OASI	2023-06-22T01:55:53	1.133	0.18	46.1	16.9	21.101 ± 0.017	20.482 ± 0.019	20.278 ± 0.018	–
675797 (2016 AX147)	OASI	2024-03-08T03:08:37	1.214	0.364	45.3	17.5	19.742 ± 0.076	19.102 ± 0.041	18.894 ± 0.05	18.951 ± 0.1
756710 (2020 GN3)	OASI	2023-09-13T01:38:34	1.083	0.117	46.8	16.5	21.407 ± 0.076	20.977 ± 0.04	20.871 ± 0.047	20.947 ± 0.087
2004 UV1	OASI	2023-11-09T03:27:33	1.123	0.235	50.5	16.8	20.104 ± 0.015	19.454 ± 0.013	19.255 ± 0.015	19.339 ± 0.035
2008 WL60	OASI	2024-04-10T04:57:31	1.284	0.357	32.7	17.6	19.853 ± 0.019	19.17 ± 0.015	18.947 ± 0.027	19.045 ± 0.086
2011 GA	OASI	2023-10-21T05:28:38	1.047	0.059	29.9	16.0	22.347 ± 0.013	21.699 ± 0.009	21.543 ± 0.011	21.947 ± 0.034
2011 YQ10	OASI	2021-10-02T02:22:59	1.078	0.122	48.3	16.5	21.287 ± 0.022	20.654 ± 0.018	20.501 ± 0.032	20.767 ± 0.123
2012 QG8	OASI	2024-05-01T22:50:55	1.241	0.235	6.9	17.0	20.106 ± 0.017	19.559 ± 0.014	19.444 ± 0.019	19.444 ± 0.053
2013 PV2	OASI	2022-12-20T01:10:49	1.084	0.115	28.7	16.8	21.874 ± 0.017	21.255 ± 0.014	21.112 ± 0.021	–
2017 UW42	CASLEO	2021-12-30T16:37:43	1.315	0.340	10.6	16.8	18.884 ± 0.032	18.373 ± 0.024	18.241 ± 0.028	18.237 ± 0.023
2019 AV4	OASI	2023-08-12T23:31:01	1.398	0.394	10.7	17.2	20.018 ± 0.014	19.467 ± 0.011	19.253 ± 0.013	19.156 ± 0.034
2020 DB5	OASI	2023-05-25T01:27:41	1.071	0.118	57.8	16.8	21.755 ± 0.014	21.09 ± 0.011	20.863 ± 0.018	21.037 ± 0.049
2021 JQ24	OASI	2021-09-01T04:33:36	1.104	0.184	54.8	16.4	20.293 ± 0.018	19.749 ± 0.014	19.63 ± 0.02	19.681 ± 0.048
2021 MO1	OASI	2021-10-09T23:13:48	1.248	0.279	23.3	17.3	19.776 ± 0.025	19.124 ± 0.022	18.916 ± 0.035	19.014 ± 0.107

Table A2. Observational circumstances and reduced magnitude for the observed NEOs. The table lists the observing site, UT date of observation, heliocentric distance (r), geocentric distance (Δ), solar phase angle (α), estimated visual magnitude (MagV). For all objects, the reduced magnitude in the V filter (m_V) is provided, with the exception of 429733 Gilbertbaker, for which the reduced magnitude is given in the R filter.

Asteroid	Observatory	Date UT	r (au)	Δ (au)	α (deg)	MagV	m_V
27031 (1998 RO4)	OASI	2023-09-08T04:37:36	1.320	0.31868	9.79	16.65	18.624 ± 0.035
	OASI	2023-09-09T23:39:56	1.326	0.326	10.05	16.72	18.689 ± 0.035
	OASI	2023-09-13T03:26:27	1.338	0.340	10.87	16.86	18.714 ± 0.035
	OASI	2023-08-21T02:44:24	1.266	0.266	15.29	16.38	18.769 ± 0.034
	OASI	2023-08-19T03:14:01	1.262	0.263	16.39	16.38	18.873 ± 0.034
	OASI	2023-08-16T00:44:43	1.255	0.259	18.14	16.39	18.959 ± 0.037
	OASI	2023-08-15T00:14:36	1.253	0.257	18.72	16.4	18.978 ± 0.034
	OASI	2023-07-25T02:30:28	1.230	0.252	28.34	16.6	19.166 ± 0.033
	OASI	2023-07-22T03:04:17	1.230	0.254	29.25	16.65	19.288 ± 0.034
88264 (2001 KN20)	OASI	2023-07-12T03:21:08	1.195	0.179	6.21	14.16	17.925 ± 0.033
	OASI	2023-07-14T04:04:32	1.191	0.177	8.46	14.22	18.042 ± 0.033
	OASI	2023-07-14T23:38:34	1.190	0.176	9.38	14.25	18.080 ± 0.034
	OASI	2023-07-18T00:02:13	1.186	0.174	12.88	14.35	18.153 ± 0.031
	OASI	2023-07-21T22:54:45	1.181	0.175	17.39	14.5	18.258 ± 0.036
	OASI	2023-08-14T00:00:53	1.186	0.219	34.8	15.53	18.547 ± 0.034
174050 (2002 CC19)	OASI	2021-02-04T23:03:21	1.145	0.160	6.25	14.42	18.113 ± 0.037
	OASI	2021-02-05T03:18:46	1.145	0.160	7.11	14.46	18.182 ± 0.034
	OASI	2021-02-05T23:18:07	1.144	0.162	11.09	14.65	18.355 ± 0.044
	OASI	2021-02-06T03:19:18	1.144	0.162	11.9	14.68	18.464 ± 0.035
	OASI	2021-02-06T22:59:31	1.144	0.16	15.71	14.85	18.581 ± 0.036
	OASI	2021-02-07T01:55:52	1.144	0.165	16.28	14.88	18.594 ± 0.036
	OASI	2021-02-10T01:16:09	1.142	0.182	28.62	15.46	18.970 ± 0.039
	OASI	2021-02-12T01:24:23	1.142	0.198	35.37	15.84	19.153 ± 0.035
326732 Nice	OASI	2021-09-12T00:50:13	1.284	0.278	3.79	15.78	17.801 ± 0.033
	OASI	2021-09-10T01:08:47	1.274	0.268	4.11	15.7	17.809 ± 0.035
	OASI	2021-09-07T22:54:33	1.264	0.258	4.86	15.64	17.914 ± 0.034
	OASI	2021-09-05T23:18:16	1.255	0.249	5.8	15.6	17.948 ± 0.033
	OASI	2021-09-02T01:18:41	1.239	0.233	8.04	15.53	18.025 ± 0.033
	OASI	2021-09-01T01:11:26	1.235	0.229	8.66	15.51	18.020 ± 0.033
	OASI	2021-10-06T02:43:56	1.420	0.439	14.29	17.45	18.453 ± 0.040
	OASI	2021-08-14T02:39:55	1.180	0.180	20.06	15.3	18.525 ± 0.034
	OASI	2021-08-12T02:37:25	1.176	0.177	21.24	15.3	18.733 ± 0.034
	OASI	2021-08-10T01:23:33	1.173	0.174	22.41	15.29	18.600 ± 0.034
	OASI	2021-08-09T02:42:57	1.171	0.173	22.92	15.29	18.575 ± 0.034
	OASI	2021-08-05T01:04:25	1.166	0.170	25.01	15.31	18.811 ± 0.031
	OASI	2021-08-03T03:45:46	1.165	0.169	25.88	15.32	18.896 ± 0.032
417581 (2006 VA3)	OASI	2021-02-04T22:39:29	1.358	0.382	11.27	16.68	17.916 ± 0.042
	OASI	2021-02-05T22:30:17	1.348	0.374	12.69	16.67	18.191 ± 0.04
	OASI	2021-02-06T22:16:47	1.337	0.366	14.4	16.67	18.398 ± 0.04
	OASI	2021-02-12T02:06:01	1.281	0.341	26.28	16.79	18.812 ± 0.036
	OASI	2021-02-12T23:52:35	1.271	0.338	28.65	16.83	18.802 ± 0.035
	OASI	2021-02-14T22:53:43	1.249	0.337	33.86	16.93	18.671 ± 0.038
	CASLEO	2023-02-24T01:42:33	1.294	0.443	38.9	17.7	18.988 ± 0.05
	OASI	2021-03-13T22:22:54	0.928	0.528	81.03	18.68	20.242 ± 0.079
429733 Gilbertbaker	OASI	2023-07-22T01:37:00	1.582	0.581	10.28	17.02	16.980 ± 0.030∗
	OASI	2023-07-19T00:17:31	1.566	0.568	11.76	17.01	17.100 ± 0.040∗
	OASI	2023-07-15T00:36:46	1.544	0.554	14.28	17.02	17.095 ± 0.030∗
	OASI	2023-07-14T04:59:24	1.54	0.552	14.85	17.02	17.095 ± 0.030∗
	OASI	2023-06-12T04:58:11	1.391	0.556	38.38	17.53	17.820 ± 0.040∗
481032 (2004 YZ23)	CASLEO	2024-06-04T 06:18:30	1.363	0.349	3.58	13.9	15.4 ± 0.25
	CASLEO	2024-06-05T02:08:22	1.375	0.362	4.40	14.0	15.34 ± 0.25
	OASI	2024-06-10T22:37:49	1.419	0.423	14.3	14.9	15.976 ± 0.033
	CASLEO	2024-05-14T06:20:11	1.226	0.411	47.97	15.5	17.05 ± 0.25
	CASLEO	2024-05-14T03:18:40	1.231	0.402	48.19	15.5	17.15 ± 0.25
620082 (2014 QL422)	OASI	2023-08-17T23:57:06	1.181	0.168	0.9	16.51	20.064 ± 0.070
	OASI	2023-08-17T23:41:09	1.18	0.168	0.9	16.51	20.083 ± 0.035
	OASI	2023-08-17T01:30:25	1.169	0.157	1.95	16.43	20.161 ± 0.035
	OASI	2023-08-15T23:40:43	1.156	0.144	3.79	16.34	20.300 ± 0.034
	OASI	2023-08-22T03:46:32	1.23	0.22	5.37	17.48	20.413 ± 0.034
	OASI	2023-08-14T23:59:06	1.144	0.132	5.75	16.24	20.392 ± 0.034
	OASI	2023-08-22T23:47:26	1.24	0.23	6.28	17.64	20.419 ± 0.037
	OASI	2023-08-24T00:39:11	1.252	0.244	7.35	17.84	20.472 ± 0.038
	OASI	2023-08-13T23:21:58	1.132	0.12	8.09	16.11	20.486 ± 0.035

Table A2 – *continued*

Asteroid	Observatory	Date UT	r (au)	Δ (au)	α (deg)	MagV	m_V
	OASI	2023-08-13T00:07:02	1.12	0.109	10.62	15.98	20.554 ± 0.034
2008 WL60	OASI	2024-05-02T01:25:28	1.423	0.424	9.86	17.47	18.774 ± 0.153
	OASI	2024-04-16T01:18:19	1.319	0.366	26.18	17.53	19.134 ± 0.133
	OASI	2024-04-13T01:28:33	1.301	0.361	29.57	17.56	19.223 ± 0.130
	OASI	2024-04-12T02:58:00	1.295	0.359	30.62	17.58	19.26 ± 0.131
	OASI	2024-04-09T05:50:14	1.278	0.356	33.8	17.62	19.282 ± 0.130
2011 YQ10	OASI	2021-12-02T01:53:52	1.34	0.357	5.72	17.95	19.735 ± 0.054
	OASI	2021-12-03T04:34:35	1.348	0.364	5.91	18.01	19.814 ± 0.065
	OASI	2021-12-08T00:31:46	1.379	0.399	7.92	18.35	19.797 ± 0.063
	OASI	2021-12-12T00:33:08	1.405	0.431	10.21	18.66	19.929 ± 0.129
	OASI	2021-10-12T01:43:08	1.096	0.147	45.3	16.85	20.794 ± 0.048
	OASI	2021-10-10T03:18:38	1.091	0.142	46.24	16.79	20.749 ± 0.038
	OASI	2021-10-08T03:19:32	1.087	0.136	47.05	16.73	20.819 ± 0.037
	CASLEO	2021-10-06T18:57:30	1.085	0.133	47.48	16.68	21.026 ± 0.032
	OASI	2021-10-06T01:54:32	1.084	0.131	47.7	16.65	20.96 ± 0.041
	CASLEO	2021-10-04T17:33:12	1.081	0.128	47.99	16.6	20.845 ± 0.02
	CASLEO	2021-10-04T17:31:55	1.081	0.128	47.99	16.6	20.79 ± 0.019
	OASI	2021-10-04T03:49:45	1.08	0.127	48.11	16.58	20.887 ± 0.034
	OASI	2021-10-02T02:41:06	1.078	0.122	48.33	16.49	20.919 ± 0.054
	OASI	2021-09-30T02:18:01	1.076	0.117	48.3	16.4	20.816 ± 0.051
2012 QG8	OASI	2024-04-14T01:41:31	1.265	0.262	1.64	16.93	19.493 ± 0.036
	OASI	2024-04-12T05:34:48	1.269	0.267	2.49	17.04	19.533 ± 0.037
	OASI	2024-04-11T04:21:50	1.271	0.27	3.01	17.1	19.588 ± 0.036
	OASI	2024-04-10T23:48:42	1.272	0.27	3.12	17.11	19.649 ± 0.046
	OASI	2024-04-06T01:41:26	1.285	0.286	5.61	17.4	19.692 ± 0.036
	OASI	2024-05-01T22:04:12	1.241	0.235	6.92	16.96	19.625 ± 0.039
	OASI	2024-05-04T01:54:52	1.24	0.234	7.82	16.99	19.663 ± 0.050
	OASI	2024-05-05T01:00:12	1.24	0.234	8.2	17.01	19.680 ± 0.050
	OASI	2024-05-13T23:57:51	1.242	0.238	11.55	17.18	19.938 ± 0.036
	CASLEO	2024-06-02T23:34:11	1.275	0.278	17.74	17.79	19.885 ± 0.100
	CASLEO	2024-06-03T23:33:54	1.278	0.281	18.02	17.83	19.986 ± 0.100
	OASI	2024-06-12T00:24:52	1.302	0.311	20.21	18.17	20.163 ± 0.049
2017 UW42	OASI	2021-12-29T16:07:32	1.318	0.342	9.92	16.79	18.67 ± 0.013
	OASI	2021-12-30T16:30:00	1.315	0.34	10.54	16.8	18.63 ± 0.019
	OASI	2022-01-04T01:07:07	1.304	0.333	13.39	16.84	18.74 ± 0.041
	OASI	2022-01-06T22:39:57	1.297	0.329	15.35	16.88	18.828 ± 0.051
	OASI	2022-02-01T01:13:54	1.267	0.343	30.13	17.37	19.157 ± 0.043
	CASLEO	2022-02-03T00:43:10	1.267	0.347	30.97	17.42	19.212 ± 0.041
	CASLEO	2022-02-05T02:34:31	1.267	0.352	31.81	17.48	19.292 ± 0.041
	CASLEO	2022-02-28T13:58:04	1.297	0.433	37.71	18.15	19.63 ± 0.023
2019 AV4	OASI	2023-08-22T04:16:24	1.337	0.327	4.53	16.44	18.311 ± 0.033
	OASI	2023-08-21T06:12:18	1.343	0.333	5.12	16.52	18.386 ± 0.041
	OASI	2023-08-17T23:06:59	1.364	0.356	7.4	16.81	18.248 ± 0.035
	OASI	2023-08-17T00:06:44	1.371	0.363	8.07	16.89	18.456 ± 0.035
	OASI	2023-08-17T23:06:59	1.364	0.356	7.4	16.81	18.496 ± 0.036
	OASI	2023-08-13T23:45:27	1.391	0.386	10.09	17.14	18.443 ± 0.037
	OASI	2023-08-12T23:15:28	1.398	0.394	10.74	17.22	18.570 ± 0.037
	OASI	2023-09-08T04:52:54	1.239	0.242	15.45	16.07	18.62 ± 0.032
	OASI	2023-09-09T23:12:14	1.23	0.236	17.65	16.08	18.734 ± 0.03
	OASI	2023-09-13T02:57:00	1.215	0.228	21.73	16.11	18.906 ± 0.03
	OASI	2023-09-14T03:25:04	1.21	0.226	23.06	16.12	19.13 ± 0.035

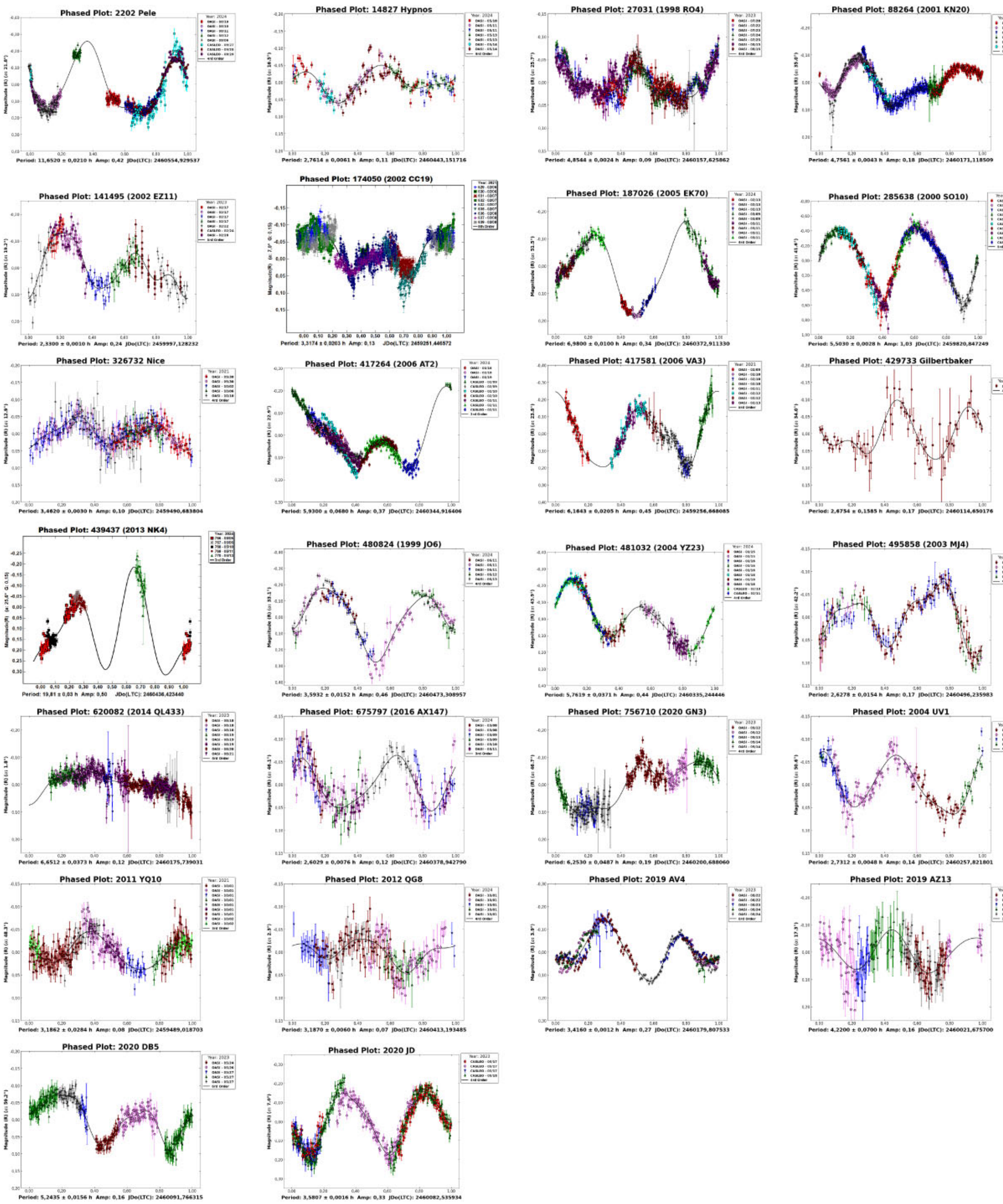

Figure A1. Composite light curves and rotation periods for 26 NEOs.

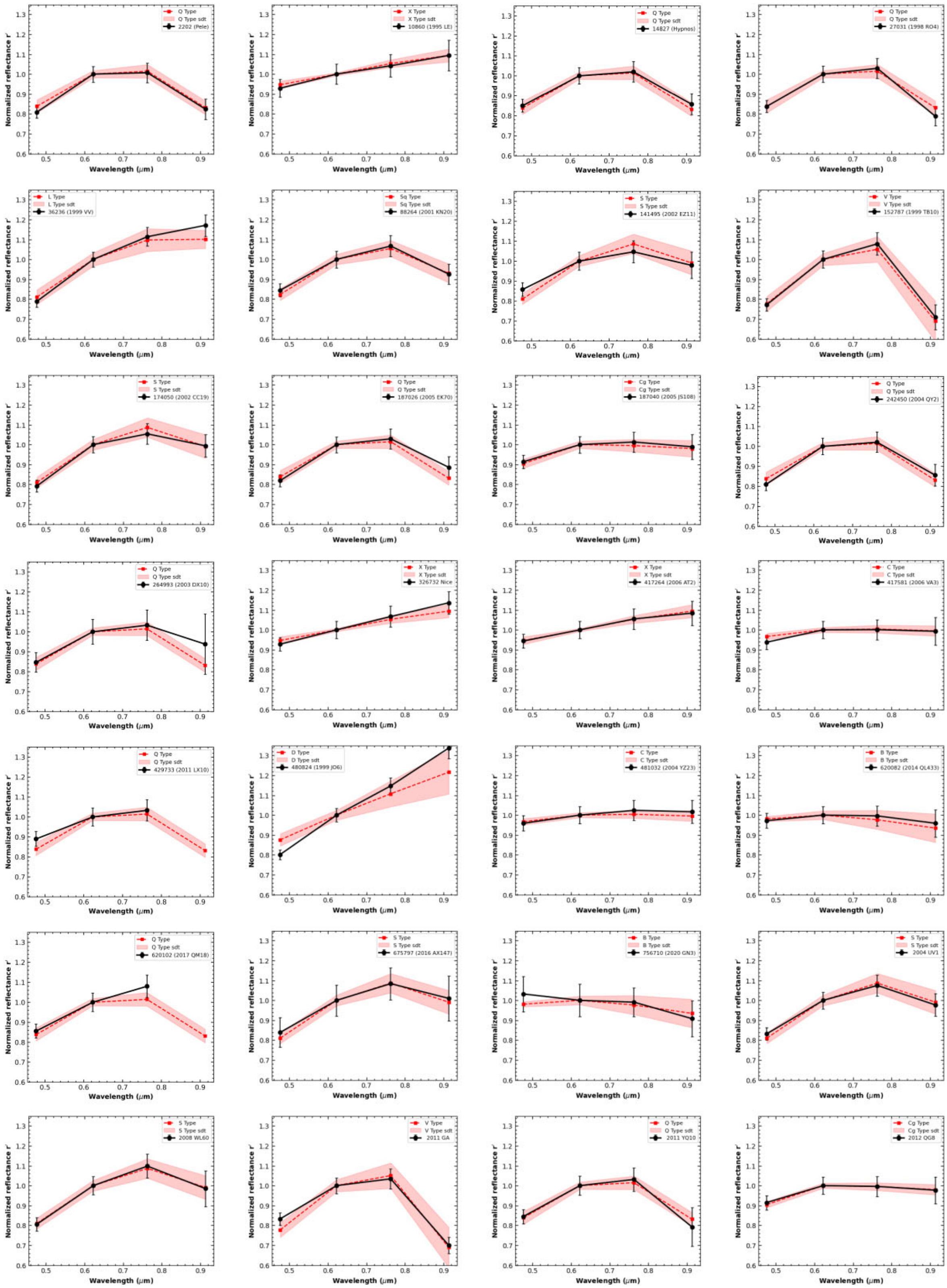

Figure A2. Photometric spectra of the observed objects, compared with interpolated mean spectra at SDSS band centres for the best-matching taxonomic class from F. E. DeMeo et al. (2009).

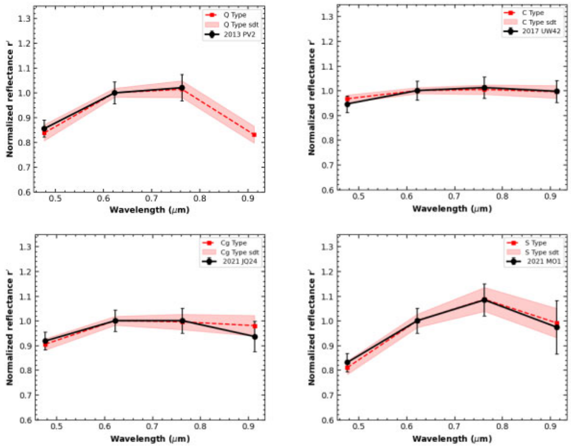

Figure A2. Continue.

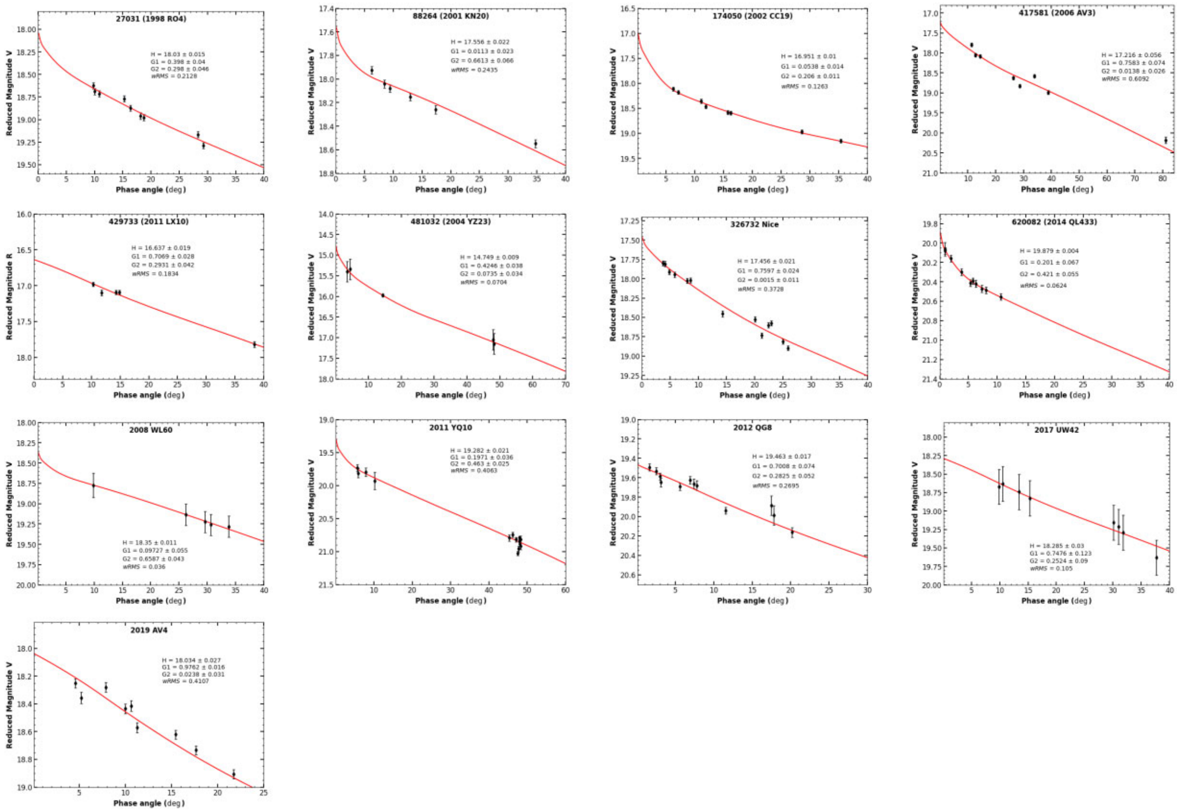

Figure A3. Phase curves of 13 NEOs. Black points show corrected reduced magnitudes with error bars; lines represent the best-fitting *H*–*G*1–*G*2 model. For NEO 429733, the phase curve was obtained in the *R* band due to the absence of *V*-band observations.

This paper has been typeset from a TEX/LATEX file prepared by the author.